

Mechanism of Thickness Dependence of Critical Current Density in HTS YBCO Film and Its Elimination Using Nano-Engineering

By

Xiang Wang

B.S., Huazhong University of Science and Technology, China, 1995

M.E., Huazhong University of Science and Technology, China, 1999

Submitted to the Department of Physics and Astronomy and the Faculty of the Graduate
School of the University of Kansas in partial fulfillment of the requirement for the degree
of Doctor of Philosophy

Dissertation Committee:

Dr. Judy Z. Wu, Committee Chair

Dr. Hui Zhao

Dr. Siyuan Han

Dr. Philip S. Baringer

Dr. Karen J. Nordheden

Date Submitted:

The dissertation committee certifies that this is the approved version of
following dissertation:

Mechanism of Thickness Dependence of Critical Current Density in HTS
YBCO Film and Its Elimination Using Nano-Engineering

Chair: Dr. Judy Z. Wu

Date approved: _____

Abstract

The most promising characteristic of a High Temperature Superconductor (HTS) is its ability to carry larger electrical current at liquid nitrogen boiling temperature and strong applied magnetic field with minimal dissipation. Numerous large scale applications such as HTS transmission cables, HTS magnets and HTS motors have been developed using HTS materials. The major limitation that prevents its wide commercialization is its high cost-to-performance ratio. However, the effort to further improve HTS current carrying capability is jeopardized by a mysterious thickness dependence of the critical current density (J_c) — J_c monotonically decreases with increasing thickness (t) at 77 K and self-field (SF). This poses a great challenge for both HTS applications and the understanding of vortex dynamics. What further complicates this issue is the complex defect structure in HTS films as well as the creep nature of magnetic vortices at a finite temperature. After a systematic study of the temperature and magnetic field effects on J_c-t , we conclude that J_c-t is most likely the result of a collective pinning effect dictated by a random pinning potential. Besides that, thermal fluctuations also alter J_c-t in a predictable way. Therefore, by either modifying the vortex structure or pinning structure, J_c-t can be eliminated. Indeed, a thin film J_c has been restored in a HTS/insulator/HTS trilayer while the magnetic coupling is weakened. Moreover, J_c-t has been removed when the random distributed point pins are overpowered by strong linear defects.

**This dissertation is dedicated to my parents, my dearest wife and
daughter**

ACKNOWLEDGEMENT

I gratefully acknowledge Drs. Judy Z Wu, Siyuan Han, Philip S Baringer, Hui Zhao, and Karen J Nordheden for serving on my dissertation committee and for their valuable guidance in the preparation of this Ph.D. dissertation. I would also like to acknowledge those who have provided guidance and assistance toward this dissertation project over the years, which include Dr. Rongtao Lu and Ms. Rose Lyn Emergo for their assistance in building the cryogenic system equipped with 8-Tesla NbTi superconducting magnet and the probe for measuring anisotropic transport properties of HTS film, my former colleagues Dr. Yiyuan Xie and Dr. Roberto S. Aga for their instrumental guidance with operating the SQUID magnetometer and conductive AFM, Mr. Jonathan R. Dizon for helping with the Labview programming of relevant electronic devices, Mr. Javier F. Baca for his collaborative contribution with sample growth and TEM analysis. A special thanks to Dr. Timothy Haugan from the Air Force Research Laboratory for the continuous exchange of ideas and providing help on countless occasions with sample fabrication and characterization.

I am indebted to my advisor, Dr. Judy Z Wu, for being a truly exceptional mentor, for providing continuous support and guidance regarding professional as well as personal matters each and every day. A special recognition goes to Dr. Alex Gurevich from the National High Magnetic Field Laboratory, who provided the important and insightful theoretical analysis of the puzzling J_c-t issue.

Finally, I want to thank all my physics colleagues for their generous support and encouragement, which makes this seven-year academic journey special and fruitful.

TABLE OF CONTENTS

| | |
|---|-------------|
| ACCEPTANCE PAGE..... | ii |
| ABSTRACT..... | iii |
| ACKNOWLEDGMENTS..... | iv |
| TABLE OF CONTENTS | vi |
| LIST OF FIGURES..... | ix |
| LIST OF SYMBOLS..... | xiii |
| ABBREVIATIONS..... | xv |
| CHAPTER 1: Introduction..... | 1 |
| 1.1 Basic Phenomena..... | 2 |
| 1.2 Early Understanding..... | 3 |
| 1.3 The BCS Theory..... | 5 |
| 1.4 The Ginzburg-Landau Theory..... | 6 |
| 1.5 Type II Superconductors..... | 8 |
| 1.6 High Temperature Superconductor..... | 10 |
| CHAPTER 2: Critical Current Density of HTS Film..... | 12 |
| 2.1 Limiting Factors of Critical Current Density..... | 13 |
| 2.2 Flux Pinning in YBCO Film..... | 16 |
| 2.3 Thermally Activated Flux Motion..... | 18 |

| | |
|--|-----------|
| 2.4 YBCO Film Fabrication and Characterization..... | 20 |
| 2.4.1 Pulsed Laser Deposition..... | 20 |
| 2.4.2 YBCO Film Characterization..... | 21 |
| 2.5 The Effect of Applied Magnetic Field on J_c..... | 25 |
| 2.6 The Effect of Temperature on J_c..... | 28 |
| 2.7 Thickness Dependence of J_c in YBCO Film..... | 29 |
| 2.8 Weak Collective Pinning Model..... | 34 |
| 2.9 Summary..... | 37 |

CHAPTER 3: The Effect of Temperature and Magnetic Field on

| | |
|--|-----------|
| Thickness Dependence of Critical Current Density..... | 38 |
| 3.1 The Effect of Temperature on J_c-t | 38 |
| 3.2 The Effect of Applied Magnetic Field on J_c-t | 43 |
| 3.3 Theoretical Analysis of J_c-t | 44 |
| 3.4 Conclusions..... | 48 |

CHAPTER 4: J_c-t Elimination Using Multilayer Approach.....

| | |
|--|----|
| 4.1 Single Vortex in S/N/S Trilayer | 50 |
| 4.2 Decoupling Vortex in YBCO/CeO ₂ /YBCO Trilayer..... | 52 |
| 4.3 Discussion..... | 56 |

| | |
|---|-----------|
| 4.4 Summary..... | 58 |
| CHAPTER 5: J_c-t Elimination Using NTP Insertion..... | 59 |
| 5.1 NTP Insertion in YBCO Film..... | 59 |
| 5.2 Microstructure Analysis of NTP | 61 |
| 5.3 J_c of YBCO Film Before and After NTP Insertion..... | 64 |
| 5.4 Conclusions..... | 68 |
| CHAPTER 6: J_c-t Elimination Using BZO NRD Insertion | 69 |
| 6.1 Growth Temperature Effect on J_c of YBCO/BZO..... | 71 |
| 6.2 Growth Temperature Effect on Pinning Structure..... | 74 |
| 6.3 Elimination of J_c - t in Low H Regime..... | 75 |
| 6.4 Lower SF J_c Observed After BZO Insertion..... | 76 |
| 6.5 Conclusions..... | 78 |
| CHAPTER 7: Conclusions and Outlook..... | 80 |
| References..... | 82 |
| Publications..... | 88 |

LIST OF FIGURES

CHAPTER 1

Fig.1.1: H - T phase diagram of a superconductor.

Fig.1.2: Comparison of flux penetration behavior between type I and type II superconductors.

Fig.1.3: The superconducting order parameter and magnetic vortex density as function of position from the center of a vortex core for an isolated vortex.

CHAPTER 2

Fig. 2.1: Plume generated by a focused pulsed UV laser beam on a YBCO target.

Fig. 2.2: I - V curves measured on a YBCO film at 77K and various fields.

Fig. 2.3: M - H hysteretic loops measured on a YBCO film at 10, 50, 77 and 86K.

Fig. 2.4: J_c as function of H measured on a same sample using traditional transport (transport J_c) and SQUID magnetization (magnetic J_c).

Fig. 2.5: J_c as function of H of a typical YBCO film plotted in a log-log scale and at various temperatures. Inset table gives the characteristic field B^* , which sets the boundary of SV regime, and α value at each given temperature.

Fig. 2.6: J_c as function of reduced temperature T/T_c measured on a typical YBCO film plotted in a semi-log scale. Solid line represents the flux-creep model predicted J_c - T dependence and T_0 is 46.8 K.

Fig. 2.7(as plotted in ref. [2.37]): J_c - t comparison between YBCO films grown on single crystal substrates and metal tape at 75K and self-field.

Fig. 2.8 (as plotted in ref. [2.38]): Milling generated J_c - d from three CC with thickness of 0.68, 3.0 and 4.7 μm . “Dead layer” is observed for two thick samples.

Fig. 2.9(data extracted from ref. [2.39]): Thickness dependence of (a) in-plane texture and out-of-plane texture; (b) critical current density and portion of a-axis orientated grain in the YBCO films grown on STO single crystal substrate.

Fig. 2.10(as plotted in ref. [2.42]): J_c as function of thickness for multilayered films (solid), plotted together with data taken on single layer YBCO films (open).

Fig. 2.11(as shown in ref.[2.42]): Cross-sectional transmission electron microscope image of a YBCO film grown on single crystal MgO substrate. A high density of defects near the YBCO/SrTiO₃ interface regarded as the dominant pinning centers is visible as a dark band.

Fig. 2.12(as plotted in ref. [2.45]): Milling generated J_c - d at 77K and different fields for (a) the 2.9 and (b) 2.0 μ m- thick films. Solid lines are fits to $J_c - t$ from as-deposited samples.

Fig. 2.13(as plotted in ref. [2.47]): J_c of as function of thickness measure at 77K and SF reported by different groups plotted in a normalized scale. Most of the data points can be more or less fitted by $1/\sqrt{t}$.

Fig. 2.14(as plotted in ref. [2.35]): Single vortex line is pinned by the collective action of many weak point-like pinning centers. In order to accommodate optimally to the pinning potential, the flux line deforms elastically by L_c , the longitudinal collective pinning length.

CHAPTER 3

Fig. 3.1: Shown is normalized M [$M/M(10K)$] as function of T for YBCO films with various thickness. Shown in the inset are the T_c and δT_c as function of thickness.

Fig. 3.2: Shown is (a) $J_c(SF) - t$ at various temperatures. The error bar corresponds to the average over different sets of samples with same thickness. (b) The reduced $J_c^r = J_c/J_c(0.6\mu m)$ as function of thickness at various temperatures. The dashed line represents the fitting of $1/t^{1/2}$.

Fig. 3.3: Shown are $J_c^r - t$ curves at (a) 77K and (b) 50K, respectively, at various H fields. The dashed line represents the fitting of $1/t^{1/2}$.

Fig. 3.4: Fig. 3.4 (as plotted in ref. [3.13]): Evolution of the J_c - t described by Eq.(3.2) for different values of (1) $\theta = 0.0065$, (2) 0.01, (3) 0.015, and (4) 0.025.

Fig. 3.5: $J_c^r(t)$ measured (squares) at 65K and 1T and calculated (blue line) from Eq.(3.1).

Fig. 3.6: $J_c^r(10K) - t$ curves at SF and 1.0 Tesla, respectively. The dashed line represents the fitting of $1/t^{1/2}$.

CHAPTER 4

Fig. 4.1: Magnetic coupling force F_c as function of insulator layer thickness t_i calculated from Eq. 4.1. The superconducting layer thickness is fixed either at 0.25 or 0.5 μm .

Fig. 4.2: J_c as function of applied magnetic field for a double sided YBCO film (0.5 μm -thick for each side) and its one side after etching of the other.

Fig. 4.3 (a) SEM and (b) conductive AFM images of a representative 0.25 μm thick YBCO film covered by 20 nm thick CeO_2 layer.

Fig. 4.4: J_c (SF, 77K) of trilayered films as function of CeO_2 thickness t_l (solid square). The solid line represents its polynomial fit. The dash-dot line corresponds to the J_c (SF, 77K) of 0.25 μm thick YBCO film.

Fig. 4.5: J_c - H curves measured on a single-layer and tri-layer films at 77K. The effective YBCO film thickness is 0.5 μm and the CeO_2 thickness t_l in the tri-layer is 20 nm.

CHAPTER 5

Fig. 5.1: SEM images of YBCO/NTP films at various thicknesses.

Fig. 5.2: SEM images of a 1.2 μm -thick YBCO/NTP film at different stages of thinning using ion milling. $R_0(1.2\mu\text{m})$ represents the original film and $R_n(d)$ represents the film after n th milling with remaining thickness d . 500nm \times 500nm grids are applied to each image and a colored pattern is used for tracking a specific NTP through different layers of thickness.

Fig. 5.3: Cross-sectional TEM of a 1.0 μm -thick NPT/YBCO film.

Fig. 5.4: J_c - t curves of YBCO standard films (circles) and YBCO/NTP films (squares) at 77 K and SF. Also shown is the J_c - t curve of YBCO/NTP (triangles) assuming a thickness-independent NTP lateral dimension. Inset shows the J_c - t curves of the two types of films in a normalized scale $J_c/J_c(0.2\mu\text{m})$. The same symbols as in Fig. 5.4 are employed for the two curves in the inset. The dash line indicates the fitting of the CP model.

Fig. 5.5: (a) J_c - t curves of YBCO/NTP films at 77 K and various H fields. Solid lines are drawn to guide eyes; (b) J_c - t of YBCO/NTP and standard YBCO films (inset) at 77 K and various H in a normalized scale $J_c/J_c(0.6\mu\text{m})$. The dash line indicates the fitting of the CP model.

CHAPTER 6

Fig. 6.1: J_c as function of applied magnetic field H for two groups of YBCO/BZO grown at 790 and 810°C at 77 K.

Fig. 6.2: J_c as function of θ , which is the angle enclosed between applied magnetic field and film normal for two representative 0.2 μm -thick YBCO/BZO films from group A and B. A similar curve measured on a 0.18 μm -thick standard YBCO film is also plotted together.

Fig. 6.3: Cross-sectional TEM images from two representative samples from group A and B. Unfortunately the TEM of group A is not very clear but several through-thickness NRD are still visible. On the other hand, the TEM image of group B sample shows dense and well aligned BZO NRDs.

Fig. 6.4: J_c as function of thickness measured on group A and B at 77 K and various magnetic fields. Solid lines and dashed lines are guides for eyes of data points from group A and group B respectively.

Fig. 6.5: J_c-T measured on two 0.6 μm -thick films with and without BZO NRD insertion. A J_c cross-over is observed at 70 K. A semi-log plot is applied to show the scaling behavior below 50 K.

LIST OF SYMBOLS

| | | |
|------------------|--|-------|
| \vec{A} | vector potential | 1.2 |
| a | numerical constant of order unity | 1.2 |
| a | inter-vortex distance | 2.5 |
| B | magnetic induction | 1.5 |
| B^* | characteristic field of single vortex pinning regime | 2.5 |
| c | velocity of light | 1.2 |
| d | remaining sample thickness | 2.7 |
| \vec{E} | electrical field vector | 1.2 |
| E_c | criteria of critical current density | 2.4.2 |
| E_l | elastic energy | 2.8 |
| E_p | pinning energy | 2.8 |
| e | proton charge | 1.2 |
| \vec{F}_L | Lorentz force | 2.1 |
| \vec{F}_p | pinning force | 2.1 |
| \vec{F}_η | friction force | 2.1 |
| F_{cm} | magnetic coupling force | 4.1 |
| \tilde{F}_{cm} | dimension-less coupling force of order unity | 4.1 |
| f_n | normal state Helmholtz free energy density | 1.1 |
| f_s | superconducting state Helmholtz free energy density | 1.1 |
| H | applied magnetic field | 1.1 |
| H_c | thermal dynamical critical field | 1.1 |
| H_{c1} | lower critical field | 1.5 |
| H_{c2} | upper critical field | 1.5 |
| \vec{h} | local magnetic flux vector | 1.2 |
| I | electrical current | 2.4.2 |
| I_c | critical current | 2.1 |
| \vec{J} | current density vector | 1.2 |
| \vec{J}_c | critical current density vector | 2.1 |
| \vec{J}_s | superconducting current density vector | 1.2 |
| J_c | critical current density | 2.1 |
| J_0 | depairing current density | 2.1 |
| L | vortex length | 2.8 |
| L_c | Larkin length | 2.8 |
| l | electron mean free path | 1.2 |
| l | sample length | 2.4.2 |
| M | magnetization | 2.4.2 |
| m | electron rest mass | 1.2 |
| n | electron density | 1.2 |

| | | |
|-----------------|--|-------|
| n_i | density of pinning center | 2.8 |
| n_s | density of superconducting electron | 1.2 |
| r_p | pin's effective radius | 2.8 |
| T | temperature | 1.1 |
| T_c | critical temperature | 1.1 |
| t | thickness | 2.7 |
| U_c | activation energy barrier | 2.3 |
| \vec{v} | vortex velocity vector | 2.1 |
| v_F | Fermi velocity | 1.2 |
| \vec{v}_s | velocity of superconducting electron | 1.4 |
| w | sample width | 2.4.2 |
| α | second order GL coefficient | 1.4 |
| α | power coefficient | 2.5 |
| β | forth order of GL coefficient | 1.4 |
| ε_l | vortex line tension | 2.8 |
| Δ | energy gap | 1.3 |
| Φ_0 | flux quanta | 1.5 |
| η | friction force coefficient | 2.1 |
| κ | GL parameter | 1.4 |
| Λ | London phenomenological parameter | 1.2 |
| λ | London penetration depth | 1.2 |
| λ_{ab} | GL penetration depth along ab-plane | 3.4 |
| λ_{GL} | GL penetration depth | 1.4 |
| τ | time | 2.3 |
| ξ | GL coherence length | 1.4 |
| ξ_0 | Pippard coherence length | 1.2 |
| ψ | GL order parameter | 1.4 |
| θ | dimensionless temperature | 3.3 |
| θ | angle enclosed between applied magnetic field and c-axis | 6.1 |
| ρ_n | normal state resistivity | 1.5 |
| ρ_{eff} | effective screen radius | 4.1 |

ABBREVIATIONS

| | | |
|-------|---|-------|
| AFM | atomic force microscopy | 4.2 |
| BCS | Bardeen-Cooper-Schrieffer | 1.3 |
| BSCCO | Bi-Sr-Ca-Cu-O superconductor | 2.1 |
| CC | coated conductor | 2.1 |
| CP | collective pinning | 2.8 |
| GL | Ginzburg-Landau | 1.4 |
| HTS | High Temperature Superconductor | 1.5 |
| LTS | Low Temperature Superconductor | 1.5 |
| NP | nano-particle | 5.1 |
| NTP | nano-tube pore | 5.1 |
| NRD | nano-rod | 6.1 |
| PLD | Pulsed Laser Deposition | 2.4.1 |
| SC | superconductor | 4.1 |
| SEM | scanning electron microscopy | 4.2 |
| SF | self-field | 2.1 |
| SV | single vortex | 2.5 |
| TAFM | thermal activated flux motion | 2.3 |
| TEM | transmission electron microscopy | 5.2 |
| YBCO | $\text{YBa}_2\text{Cu}_3\text{O}_{7-x}$ | 1.6 |
| XRD | X-ray diffraction | 2.4.2 |
| ZFC | zero-field-cooled | 3.1 |
| 2G | second generation | 2.1 |

CHAPTER 1: Introduction

In 1911, just 3 years after he had first liquefied helium, superconductivity was first discovered by H. Kamerlingh Onnes in Leiden ^[1.1]. What he observed was the complete disappearance of electrical resistance in various metals when temperature was reduced below a critical temperature T_c . Followed by the monumental discovery, a more fundamental phenomenon of superconductivity has been revealed by Meissner and Ochsenfeld in 1933 when they observed that a superconductor completely expels a weak applied magnetic field from interior except for a thin layer at the surface ^[1.2]. This remarkable phenomenon has attracted many scientists since then and still remains fascinating after nearly a century of investigation. In 1955, a fundamental understanding of superconductivity and satisfactory theoretical picture called BCS model emerged ^[1.3]. However the upper limit of T_c predicted by the original BCS model was about 30 K and by 1973, the highest T_c observed was only 23.3 K found on Nb₃Ge. This situation was overturned and revitalized in 1986, when a new class of high-temperature superconductor (HTS) with critical temperature T_c of 35 K, a 12 K above the old record, was discovered by Bednorz and Müller^[1.4]. This sparked an worldwide effort for searching superconductors with even higher T_c . In 1987, C. W. Chu and Maw-Kuen Wu first demonstrated that YBa₂Cu₃O_{7-x} has T_c of 93 K. This discovery is of great importance for HTS power-related application owing to this high T_c , which leads a significant reduction of cryogenic cost.

1.1 Basic phenomena

The complete disappearance of electrical resistance of certain metals such as mercury, lead and tin below their T_c , observed by Kamerlingh Onnes in 1911, suggests that a persistent current could flow without measurable decrease for a long period. In fact, as suggested by nuclear resonance measurement, one shall expect absolutely no change in the persistent current in time less than 10^{10} years. Therefore, literally in superconducting state, material displays perfect conductivity (DC) which is regarded as the first traditional hallmark of superconductivity.

The second hallmark is the perfect diamagnetism, discovered in 1933 by Meissner and Ochsenfel. They found that not only a magnetic field is excluded from entering a superconductor, as might seem to be explained by perfect conductivity, but also is expelled from an originally normal sample as it is cooled through T_c . This, of course, could not be explained by perfect conductivity, which would tend to trap flux in. The existence of Meissner effect implies that superconductivity could be destroyed by a critical magnetic field H_c which is thermodynamically related to the free-energy difference between the normal

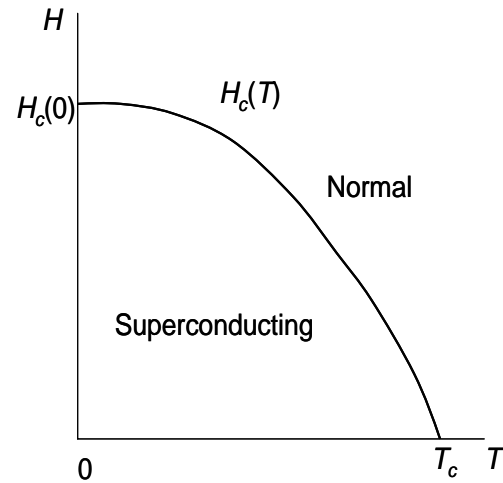


Fig.1.1: H - T phase diagram of a superconductor.

and superconducting states. This energy difference is called the condensation energy of superconducting state and quantitatively H_c is determined by

$$\frac{H_c^2(T)}{8\pi} = f_n(T) - f_s(T) \quad (1.1)$$

where f_n and f_s are the Helmholtz free energies per volume in the respective phases at zero field. Empirically $H_c(T)$ can be well approximated by a parabolic law

$$H_c(T) \approx H_c(0)[1 - (T/T_c)^2] \quad (1.2)$$

illustrated in Fig. 1.1.

1.2 Early understanding

In 1935 the brothers of F. and H. London proposed two equations which well described the two basic electrodynamics properties ^[1.5]: the perfect conductivity and perfect diamagnetism. Microscopically, the electrical and magnetic response of a superconductor can be written as

$$\vec{E} = \frac{\partial}{\partial t}(\Lambda \vec{J}_s) \quad (1.3)$$

$$\vec{h} = -c\nabla \times (\Lambda \vec{J}_s) \quad (1.4)$$

where

$$\Lambda = 4\pi\lambda^2 / c^2 = m / n_s e^2 \quad (1.5)$$

is a phenomenological parameter. \vec{E} and \vec{h} denote the value of local electrical field and flux density, respectively. n_s represents the density of superconducting electrons and \vec{J}_s ,

the superconducting current density. Eq. (1.3) describe perfect conductivity and Eq. (1.4), when combined with the Maxwell equation $\nabla \times \vec{h} = 4\pi\vec{J} / c$, leads to

$$\nabla^2 \vec{h} = \vec{h} / \lambda^2 \quad (1.6)$$

This simply suggests that a magnetic field is exponentially screened from the interior of a superconductor with a penetration depth λ . Using the total density of electron n as the natural limit n_s , one obtains the λ as T approaches 0 K

$$\lambda(0) = (mc^2 / 4\pi ne^2)^{1/2} \quad (1.7)$$

However, experimentally measured λ is always larger than this theoretic prediction even after and extrapolation to 0 K.

Pippard proposed a nonlocal generalization of London equation in attempt to explain the shorter λ observed experimentally ^[1.6]. Based on an uncertainty-principle argument, he argued that the superconducting wave function should have a characteristic dimension ξ_0 called as Pippard coherent length

$$\xi_0 = a \frac{\hbar v_F}{kT_c} \quad (1.8)$$

where a is a numerical constant of order unity and v_F is the Fermi velocity. Physically ξ_0 can be viewed as the smallest size of the wave packet which is formed by the superconducting electrons. For typical elemental superconductors such as tin and aluminum, $\xi_0 \gg \lambda(0)$. The core equation of Pippard nonlocal theory can be written as

$$\vec{J}_s(\vec{r}) = -\frac{3}{4\pi\xi_0\Lambda c} \int \frac{\vec{R}[\vec{R} \cdot \vec{A}(\vec{r}')] }{R^4} e^{-R/\xi} d\vec{r}' \quad (1.9)$$

in replacement of the original London expression

$$\vec{J}_s = \frac{-\vec{A}}{\Lambda c} \quad (1.10)$$

where $\vec{R} = \vec{r} - \vec{r}'$ and \vec{A} is the vector potential. The coherence length ξ in a dirty superconductor is related to the clean limit ξ_0 through

$$\frac{1}{\xi} = \frac{1}{\xi_0} + \frac{1}{l} \quad (1.11)$$

where l is the mean free path. Not only Pippard's nonlocal theory can fit the experimental data, but it also has the similar electrodynamics form expected from the microscopic theory found four years later.

1.3 The BCS theory

The establishment of BCS theory represents one of the most important understandings of superconductivity. After several major experiments demonstrated the existence of an energy gap Δ , of order of kT_c , between the ground state and the quasi-particle excitations of the system, Bardeen, Cooper, and Schrieffer produced their pairing theory (BCS theory) of superconductivity. In this theory, they showed that even a weak attractive interaction between electrons would cause instability of the ordinary Fermi-sea ground state. Therefore electrons are pairing up through the second order electron-phonon interaction. These so-called Cooper pairs have a spatial extension of Pippard coherent length ξ_0 and comprise the superconducting charges from the early phenomenological theories.

The BCS theory predicts that, in order to break up the Cooper pair, minimum energy of $2\Delta(T)$ should be applied. The $\Delta(T)$ was predicted to increase from zero at T_c to

a maximum value $\Delta(0) = 1.764kT_c$ at $T \ll T_c$. Note that even though the BCS theory gives an excellent account of the situation where Δ is a constant in space, it is not applicable to those situations in which the existence of spatial inhomogeneity is of the entire interest.

1.4 The Ginzburg-Landau theory

Concentrating entirely on the superconducting electrons rather than on excitations, Ginzburg and Landau proposed the Ginzburg-Landau (GL) theory in 1950, 7 years before the BCS theory^[1.7]. The core concept of GL theory is the superconducting electrons can be described by complex pseudowave function ψ , and the local density of the superconducting electrons n_s is given by $|\psi(x)|^2$. The basic postulate of GL theory is that, under the assumption ψ is small and varies slowly in space, the free energy density f can be expanded in a series of the form

$$f = f_n + \alpha |\psi|^2 + \frac{\beta}{2} |\psi|^4 + \frac{1}{2m^*} \left| \left(\frac{\hbar}{i} \nabla - \frac{e^*}{c} \vec{A} \right) \psi \right|^2 + \frac{h^2}{8\pi} \quad (1.12)$$

Using variation method, Eq. (1.12) leads to the famous GL differential equations

$$\alpha \psi + \beta |\psi|^2 \psi + \frac{1}{2m^*} \left(\frac{\hbar}{i} \nabla - \frac{e^*}{c} \vec{A} \right)^2 \psi = 0 \quad (1.13)$$

and
$$\vec{J} = \frac{e^*}{m^*} |\psi|^2 \left(\hbar \nabla \psi - \frac{e^*}{c} \vec{A} \right) = e^* |\psi|^2 \vec{v}_s \quad (1.14)$$

Combining the GL theory and London equations, one obtains the penetration depth

$$\lambda_{GL}^2 = \frac{m^* c^2}{4\pi |\psi|^2 e^{*2}} \quad (1.15)$$

Considering the pairing of electron and replacing all the starred parameter by the free electron value, for example $m^*=2m$, $e^*=2e$ and $|\psi|^2 = n_s^* = n_s / 2$, it is not hard to find that London penetration depth is not changed by the pairing. The other important characteristic length, so called the GL coherence length $\xi_{GL}(T)$, can be obtained from the simplified one dimensional GL Eq. (1.13)

$$\xi_{GL}^2(T) \frac{d^2 f}{dx^2} + f - f^3 = 0 \quad (1.16)$$

where $f = \psi / \psi_\infty$. Solve the Eq. (1.16), one can find that

$$f(x) \sim 1 - e^{\pm \sqrt{2}x / \xi_{GL}(T)} \quad (1.17)$$

This shows that a small disturbance of ψ from ψ_∞ will decay in a characteristic length of order $\xi(T)$

$$\xi_{GL}^2(T) = \frac{\hbar^2}{2m^* |\alpha(T)|} \propto \frac{1}{1 - T / T_c} \quad (1.18)$$

Note that $\xi_{GL}(T)$ physically differs from Pippard's ξ and $\xi_{GL}(T)$ diverges at T_c , whereas the electrodynamic ξ is essentially constant. Nevertheless, I will retain this traditional notation in rest of this dissertation. Since all the theoretic discussion is within the GL theory hereafter, ξ and λ are only used for the two GL characteristic lengths if it is not specifically pointed out.

As soon as λ and ξ are defined, one can find the famous dimensionless GL parameter κ ,

$$\kappa = \frac{\lambda(T)}{\xi(T)} = \frac{2\sqrt{2}H_c(T)\lambda^2(T)}{\Phi_0} \quad (1.19)$$

where $\Phi_0 = \frac{\pi\hbar}{e}$ is the flux quanta. For typical classic pure superconductor, also called Type I superconductor, $\kappa \ll 1$ and there is a positive surface energy associated with interface between normal and superconducting region.

1.5 Type II superconductors

In 1957, Abrikosov published an important paper regarding the possible existence of another type of superconductor ^[1.8]. He investigated the scenario of $\kappa \gg 1$ within the GL framework and found that this type of superconductor could have very different properties from the Type I superconductor. Abrikosov called it type II superconductor to distinguish it from

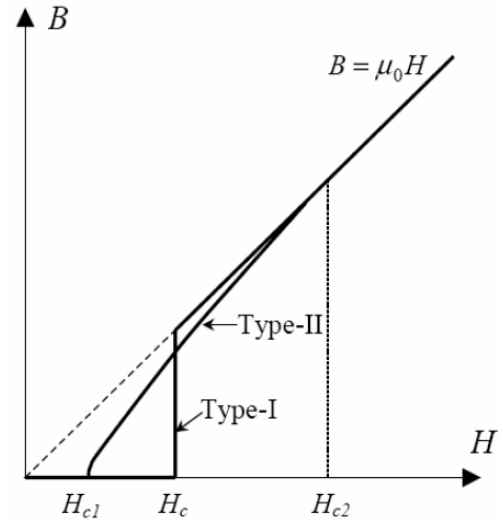


Fig.1.2: Comparison of flux penetration behavior between type I and type II superconductors.

the early type I variety. He also showed the exact break point between the two regimes was at $\kappa = 1/\sqrt{2}$. For superconductor with $\kappa > 1/\sqrt{2}$, he found the diamagnetism could be partially maintained even at $H > H_c$. In another word, instead of discontinuous breakdown of superconductivity in a first-order transition at H_c for type I superconductor, for type II superconductor, there is a continuous increase in flux penetration starting at a

lower critical field H_{c1} and reaching $B = H$ at an upper critical field H_{c2} , as shown schematically in Fig. 1.2. Another important result of Abrikosov's analysis is that, in the regime of $H_{c2} > H > H_{c1}$, so called mixed state, flux penetrates inside in a regular array of flux tubes, each carrying a flux quanta $\Phi_0 = 2.07 \times 10^{-7} \text{G-cm}^2$. Each flux quanta Φ_0 , as illustrated in Fig.

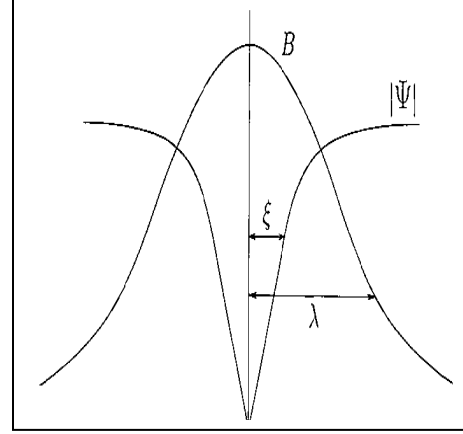


Fig.1.3: The superconducting order parameter and magnetic vortex density as function of position from the center of a vortex core for an isolated vortex

1.3, has a cylindrical core which is

surrounded by screening current. The circulating screening current, which is just necessary to generate one flux quanta, also forms a hollow cylinder with thickness of λ .

The core has a radius about ξ where the order parameter ($|\psi|$) drops from unit to zero as it approaches the center. Therefore there is no energy gap in the cores and theoretically the perfect conductivity would be lost in an ideal homogenous type II superconductor at $H >$

H_{c1} . In the presence of a transport current J , the vortex tubes experience Lorentz force $J\Phi_0/c$ per unit length which tends to drive them sideways and induces a longitudinal resistive voltage. In this situation, Bardeen and Stephen showed that this dissipation procedure is only resisted by a viscous drag and the ideal type II superconductor should

show a resistance of $\rho_n \frac{B}{H_{c2}}$ (ρ_n is the resistivity at normal state) ^[1.9]. However, in real

material, due to its relatively small ξ , any inhomogeneity at the same order of ξ , can pin the flux, so that there is essentially no resistance until a finite current is reached and the

Lorentz force exceeds the pinning force. Therefore the whole business in terms of superconductor application is to make the material “imperfect” in a specific way rather than retaining a perfect material.

Unlike Type I superconductors, Type II superconductors typically can have a H_{c2} as high as several tens of Tesla. Since the superconducting electrical property can be maintained within H_{c2} with introduction of pinning centers, many large-scale applications such as superconducting magnet have been developed on conventional Type II superconductors. To distinguish from the later discovered Type II superconductor with T_c higher than 30 K (HTS), the conventional Type II superconductor is also called low T_c superconductor (LTS).

1.6 High Temperature superconductivity

In 1986, Bednorz and Müller discovered the high T_c ($\sim 35\text{K}$) superconductivity in layered material LBCO dominated by copper oxide planes, for which they were awarded the Nobel Prize in 1987. This discovery was surprising and exciting not only because of the high T_c , but also because it revealed the great potential of a new class of oxide superconductor. A big jump of $T_c \sim 90\text{K}$ immediately followed, with the discovery of $\text{YBa}_2\text{Cu}_3\text{O}_{7-x}$ (YBCO) nearly simultaneously by groups in the United States and China ^[1.10]. As of this point, the highest $T_c \sim 135\text{K}$ is found on mercury based HTS material and this value can be further increased to $\sim 164\text{K}$ if pressurized.

The discovery of HTS provides a great potential for industrial application as well as a rich physical system for material science. With T_c above liquid nitrogen boiling

temperature, it has opened the way to a broader range of practical application than for the traditional low T_c superconductor simply because cooling can be realized by readily available liquid nitrogen. However, the ceramic nature of the cuprates also poses great challenges to material scientists for several reasons: (1) It is hard to fabricate in useful forms due to its brittle nature; (2) the high T_c combines with low v_F results in a short ξ and allows stronger fluctuations; (3) the anisotropy induced by layered structure reduces the integrity of vortex lines as well as the efficiency of pinning. Despite all these formidable obstacles, great accomplishments have been achieved in the past twenty years. In the next chapter, we will briefly review the progress of HTS application, especially on the aspect of power-related applications.

CHAPTER 2: Critical Current Density of HTS Film

Since the discovery of HTS, the promise of non-dissipation devices operating at liquid-nitrogen temperature has stimulated a worldwide research tide. One of the most prominent aspects is the application in the electric power area such as magnet, motors and transmission lines. In order to make this ceramic material into a long, strong and flexible conductor like copper wire, the first solution was to pack Bi-Sr-Ca-Cu-O(BSCCO) superconducting powder into a silver tube^[2.1]. Following a series of rolling, annealing sequences and the final product was a 4-mm-wide flexible tape which can carry the critical current over 100 A at 77 K. This so-called first-generation (1G) HTS cable is widely used in the present-day HTS industry. However, the 1G HTS cable fabrication heavily relies on the use of silver which makes it too expensive for most of the commercial application. Another major setback comes from the intrinsic high anisotropy of the BSCCO material itself, which strongly limits its current carrying capability with even moderate magnetic field presence.

In the early 1990s, an alternative approach using thin-film epitaxy was conceived^[2.2]. This so-called second-generation coated conductor (CC) uses physical or chemical procedures coating a thin epitaxial layer of HTS on metal tape. This process needs very little silver and make the economy-of-scale cost reduction is possible. Also the in-field behavior was improved because of the relatively weak anisotropy of YBCO compound, which is regarded as the major candidate of 2G HTS CC. At this point, three companies already demonstrated the great potential of 2G YBCO CC by recent announcement of successful fabrication of YBCO tapes more than 100 meters long,

carrying 200A/cm-width at 77K ^[2.3-2.5]. SuperPower, one of these companies, has delivered 10 km of YBCO CC for a power-distribution cable project in Albany, New York ^[2.6]. The similar amount of YBCO CC was also delivered by another company, American Superconductor, including two fault-current-limiter demonstrations. The current cost (\$/KA-m) of YBCO CC is about ten times of copper wire(~60\$/KA-m) but the gap is closing rapidly as the industries gear up for large scale application. Even with such remarkable progress, the mission is still not accomplished. The challenge arises from two important areas: performance in thick HTS film and at high applied magnetic field. In another words, is there any potential existing to substantially reduce the cost/performance ratio, and increase odds of commercial success? To answer this question, first we have to go back to the fundamental property of HTS.

2.1 Limiting Factors of Critical Current Density

The fundamental property that makes superconductors attractive in power-related applications is the ability to carry large current without any dissipation. However, theoretically the zero dissipation is limited to a critical quantity, so-called critical current density J_c . With a defined cross section area A , J_c translates to critical current I_c by $I_c = AJ_c$. Therefore, understanding the major factors affecting J_c has been the central issue for the HTS CC community.

From theoretical point of view, the superconducting current J_s can be expressed in the simple form of Eq. (1.14) within GL theory. This allows us to simplify the free-energy expression Eq. (1.12) as

$$f = f_n + \alpha |\psi|^2 + \frac{\beta}{2} |\psi|^4 + |\psi|^2 \frac{1}{2} m^* v_s^2 + \frac{h^2}{8\pi} \quad (2.1)$$

Use Eq. (2.1) to treat the case of a uniform current density though a thin film or wire with transverse dimension much less than the penetration depth λ , for a given v_s , we can minimize Eq. (2.1) to find the optimum value of $|\psi|^2$. The result can be written as

$$J_s = 2e |\psi|^2 v_s = 2e \psi_\infty^2 \left(1 - \frac{m v_s^2}{2 |\alpha|}\right) v_s \quad (2.2)$$

It is not hard to find J_s maximizes itself when $m v_s^2 = |\alpha|/3$ and $|\psi|^2 = \frac{2}{3} \psi_\infty^2$. Plug these into Eq (2.2), we obtain the critical current density J_c and its temperature dependence

$$J_c = \frac{4}{3} e \psi_\infty^2 \left(\frac{|\alpha|}{3m}\right)^{1/2} = \frac{c H_c(T)}{3 \sqrt{6\pi} \lambda(T)} \propto \left(1 - \frac{T}{T_c}\right)^{3/2} \quad (2.3)$$

Despite complication given by the nonlinear treatment shown above, thermodynamically, the critical current density J_c can be obtained by equating the density of kinetic energy to that of condensation energy using the London descriptions

$$\frac{1}{2} n_s m v_c^2 = \frac{2\pi}{c^2} \lambda^2 J_c^2 = \frac{H_c^2}{8\pi} \quad (2.4)$$

and one obtains $J_c = cH_c/4\pi\lambda$. This value exceeds GL result (2.3) by a factor of 1.84 because it fails to take into account the decrease in $|\psi|^2$ with increasing current density. Nevertheless, the above mentioned J_c poses the theoretic limit J_0 , the so-called “depairing limit” for a thin uniform superconductor since superconductivity is associated with the pairing of carriers.

Due to the small lower critical field H_{c1} of HTS (and also type II superconductor), a small amount of transporting current in the order of several tenth of the depairing J_c will generate a self-field (SF) large enough to drive the system into mixed state. When an external current \vec{J} is applied to the vortex system, the vortex experiences the Lorentz force per volume

$$\vec{F}_L = -\vec{J} \times \vec{B} / c \quad (2.5)$$

Within a perfect homogeneous system, this F_L is only counteracted by the friction force

$$\vec{F}_\eta = -\eta \vec{v} \quad (2.6)$$

where $\vec{v} = \vec{B} \times \vec{J} / c\eta$ is the steady-state velocity of the vortex system. The dissipation arises due to the finite electrical field

$$\vec{E} = \vec{B} \times \vec{v} / c \quad (2.7)$$

generated as the consequence of vortex motion. Since J and E are anti-parallel, the power

$$P = (\vec{J} \times \vec{B})^2 / c^2 \eta \quad (2.8)$$

is dissipated and the property of transporting dissipation-free current is lost. In order to recover the desired property of dissipation-free current flow, the vortex has to be pinned. Therefore, the critical state in the mixed state is described by the equilibrium between the Lorentz force F_L and pinning force F_P

$$\vec{F}_L = \vec{J}_c \times \vec{B} / c = -\vec{F}_P \quad (2.9)$$

and the $J_c = cF_P/B$ sets the depinning limit of the transporting current. Fortunately, in real material, due to the relatively small ξ , any inhomogeneity at the same order of ξ affects the order parameter and contributes to the finite pinning force F_P , and thereby the technological usefulness of Type II superconductor is recovered. Hence, improving supercurrent carrying capability has become a matter of optimizing the pinning structure.

2.2 Flux Pinning in YBCO Film

Pinning arises from the localized material defects, crystalline imperfection and secondary phase. Since the G-L coherence length ξ of HTS material are typically in the order of nanometer, any defect with dimension larger than that could be potential pinning center. Owing to the large number of defects naturally generated during the thin-film growth, YBCO thin film usually has J_c one to two orders of higher than that of single crystal.

Depending on its distribution and orientation within the SC matrix, the pinning itself can be divided into two groups. One is correlated pinning and the other random

pinning. Correlated pinning arises from approximately parallel arrays of extended linear or planar defects. Their effect becomes the most strong when the applied magnetic field is aligned with them. The correlated pinning decreases with the increasing misalignment between the defects and vortices. So the signature of correlated pinning is a peak in the angular dependence of J_c . For example, the typical HTS has a layer structure consisting alternative strong superconducting layers (ab-plane) and weak superconducting layers ^[2.7]. This layered structure results in a strong modulation of order parameter and hence provides a preferential pinning for magnetic flux B parallel to them. It has been confirmed that this preferential pinning, so called “intrinsic pinning”, contributes the angular dependence of J_c ^[2.8]. There are some additional planar defects related to imperfect epitaxial growth such as stacking faults and twin boundaries which could also provide directional pinning enhancement as B parallel to them. It is also suggested that linear growth defect which threads through film thickness, such as edge and screw dislocations could play an important role for the observed high J_c in YBCO films ^[2.9, 2.10]. Sequential etching experiments by Dam *et al* showed a “characteristic field”, beyond which J_c drops with increasing field, is correlated with the surface density of screw dislocations ^[2.11]. “Random” or “uncorrelated pinning” is due to randomly distributed localized defects, which are generally point-like defects and in this case the pinning is relatively uniform for all field orientations. Among those point-like defects, foremost are the oxygen vacancies in the strongly superconducting CuO_2 plane (ab-plane) ^[2.12]. Such atomic size vacancies are potentially pinning centers due to the small ξ of HTS material. It is also suggested that large point defects, usually are sparse insulating or normal metallic secondary-phase inclusions (Y_2O_3 , Y124), could provide strong pinning in

YBCO films ^[2.13]. These defects, typically with diameter $\sim 10 - 20$ nm and density $\sim 10^{21} - 10^{23} \text{ m}^{-3}$, are known to exist in sputter-deposited ^[2.14, 2.15], pulsed laser deposited ^[2.16] and solution-based metal organic deposited YBCO films ^[2.17]. Some authors also reported observation of high J_c in porous YBCO films grown on miscut substrates ^[2.18]. It is suggested that these pores could provide strong correlated pinning which improves J_c at low field.

Unfortunately the HTS community has not reached a consensus regarding the dominant pinning centers in typical as-grown YBCO films yet. This diversification brings difficulty to directly correlate J_c with certain type of defect since pinning is not simply additive. What further complicates J_c is the pronounced thermal fluctuation of flux, which is inherently associated with the anisotropic nature of HTS material.

2.3 Thermally Activated Flux Motion

The technologically most interesting property of HTS is its ability to carry a bulk current density \vec{J} with essentially no dissipation. This current density is determined by the magnetic flux density gradient via Maxwell's equation

$$\nabla \times \vec{B} = (4\pi / c)\vec{J} \quad (2.10)$$

Therefore a YBCO film carrying a transport current at a finite temperature is only in a metastable state from a thermodynamic point of view. In another word, this current is bound to decay due to thermally activated flux motion (TAFM). This phenomenon is also

known as flux creep and was first introduced by Anderson in 1962 ^[2.19]. At a finite temperature T , Anderson's flux creep model leads to the famous logarithmic time (τ) decay of the critical (diamagnetic) current J_c ,

$$J(\tau) = J_c \left[1 - \frac{T}{U_c} \ln(1 + \tau / \tau_0) \right] \quad (2.11)$$

where τ_0 is a time constant determined by pinning structure and U_c is the energy barrier against thermally activated flux motion. Typical U_c obtained in magnetic relaxation experiments are in the range of 100-1000 K ^[2.20]. The decay coefficients T/U_c of LTS, in the case in which J is close to its critical value J_c , are of the order of 10^{-3} ^[2.21]. However, in the HTS material such as YBCO single crystal, the decay coefficients turn out to be much larger, reaching even the order of 5% at 20 K ^[2.22]. This large logarithmic decay rate is the result of several factors such as the small U_c , which is the consequence of small ξ , and the large anisotropy due to the HTS layered structure. If combining with the typical time factor τ/τ_0 in the order of 20 (assuming waiting time $\tau = 60$ seconds), this large decay rate leads to an approximately halved experimentally measured current density due to the flux creep, as compared with the J_c predicted from critical state even at a low $T \sim 10$ K. Therefore for practical situation, besides pinning behavior, TAFM is the other dominant factor dictating J_c . Since thermal creep could have occurred much earlier before the critical state, it is worth knowing that determination of critical current density of HTS material is not trivial. Precautions have to be taken to interpret reported J_c values since various characterization techniques usually give very different J_c 's even on the same sample.

2.4 YBCO Film Fabrication and Characterization

2.4.1 Pulsed Laser Deposition

Pulsed Laser Deposition (PLD) plays a prominent role in the fabrication of HTS CC and record numbers of J_c and I_c have been achieved using this method. As a major method for depositing films of complex material, PLD has been well established since its first introduction by Smith and Turner in 1965 [2.23]. The real breakthrough of PLD fabrication of epitaxial HTS films was made at Bell Communications Research by Dijkkamp in 1987 [2.24]. Conceptually, the process of PLD is very simple and the fabrication can be well controlled by adjusting several critical parameters such as growth temperature, oxygen partial pressure and laser energy density. Therefore it serves as the major YBCO film fabrication technique in this dissertation study. During the fabrication process, a pulsed ultraviolet (UV) laser (wave length is 248 nm) beam

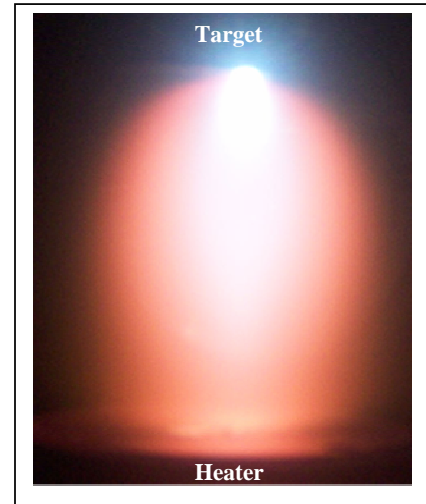


Fig. 2.1: plume generated by a focused pulsed UV laser beam on a YBCO target.

is generated by the Lambda Excimer Laser (COMPex 205) and directed into the vacuum chamber through a UV transparent window and two UV mirrors. The raw laser beam has the output energy about 200 mJ. This beam is then focused onto the target surface into a $3.5 \times 1.5 \text{ mm}^2$ spot with the energy density $\sim 3.2 \text{ J/cm}^2$ by a lens outside the vacuum chamber. Since in most of the materials, the UV laser energy is absorbed only by the outermost layer of the target with thickness less than 100 nm, combining this

phenomenon with the extremely short pulse duration less than 50 ns, this high energy density causes the local surface temperature to rise up to thousands of degrees of Celsius ($^{\circ}\text{C}$) and evaporate a small amount of target material in a very short time. Such non-equilibrium heating process generates a flash of evaporated material called a plume that deposits on a substrate, producing a film with identical cations composition as the target surface. During the YBCO film growth, the substrate's temperature is held at 760-790 $^{\circ}\text{C}$ and the oxygen pressure is dynamically controlled at 230 to 300 mTorr by a throttle valve. Following the deposition, the film is further oxygenated at 490 $^{\circ}\text{C}$ for 50 minutes to realize a phase transition from a non-superconducting tetragonal phase to superconducting orthorhombic phase.

Since PLD offers one effective method to “photocopy” target composition into thin film, it has been widely applied by researchers to systematically incorporate defects in YBCO films. Specific approaches such as substrate surface decoration ^[2.25, 2.26], impurity additions ^[2.27, 2.28], rare-earth addition and/or substitutions ^[2.29, 2.30] have been made using PLD in the past five years and many exciting results have been obtained. Construction of multilayer structure can also be realized using PLD by simply positioning different targets under the laser beam.

2.4.2 YBCO Film Characterization

It is well known that large angle grain boundary greatly suppresses J_c since the strong coupling only occurs when the ab-planes are well aligned. This necessitates the epitaxial growth of YBCO film if its high critical current carrying capability for power-related applications is desired. The most powerful tool for characterizing crystallinity is

X-ray diffraction (XRD), which is also the major characterization technique for microstructure analysis in this work. Under carefully optimized growth condition, the PLD YBCO films are c-axis oriented epitaxial films with their a-axis and/or b-axis well aligned in plane with the (100) and (010) axes of the single crystal substrates.

Obviously the most interesting quantities in term of HTS application are its superconducting properties such as T_c and J_c . The superconductivity properties are characterized with either electrical transport method or magnetization using SQUID magnetometer. Determination of T_c is rather straight forward and both techniques give consistent results. However, J_c characterization involves complications owing to the flux creep nature of HTS material, even though both techniques originated from the same principle — movement of flux lines generates an electrical field E and leads to *observable* dissipation. Regarding each individual technique, the transport measurement is viewed as a simple model-free means to characterize J_c via the I - V characteristics. The typical I - V curves measured on a 500 x 20 μm micro-bridge patterned from a 0.3 μm -thick YBCO film is shown in Fig. 2.2. The measurement was conducted at 77 K and various magnetic fields. The criteria of J_c was chosen as $E_c = 1 \mu\text{V/cm}$ which is typically

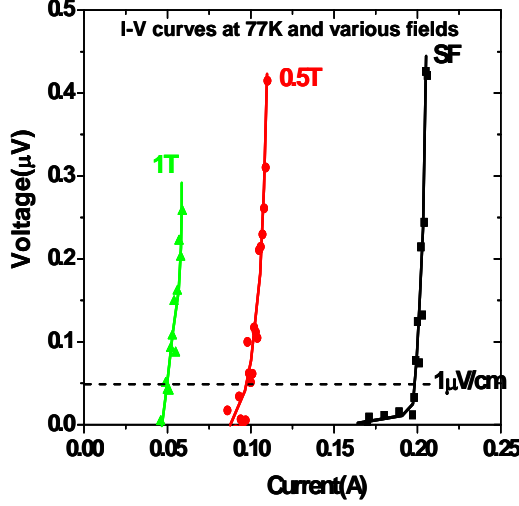


Fig. 2.2: I - V curves measured on a YBCO film at 77K and various fields.

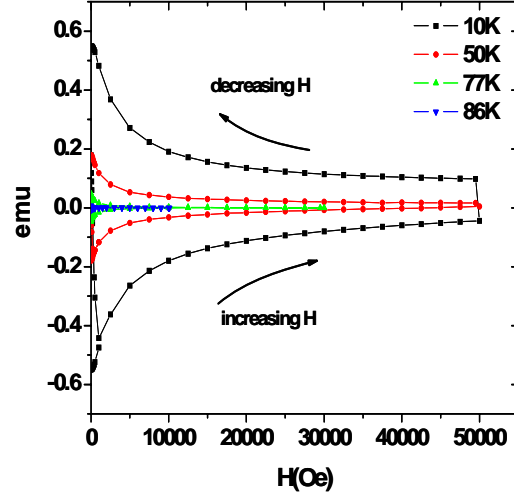


Fig. 2.3: M - H hysteretic loops measured on a YBCO film at 10, 50, 77 and 86K.

applied by the majority of the HTS community. As for magnetic characterization, due to the restraining force F_p is always against flux motion, the flux density gradient is then established across the sample. It causes hysteresis of the magnetic moment (M) during the magnetization of a hard superconductor. Hysteretic loops measured on a 0.25 μm -thick YBCO film at various temperatures are shown in Fig. 2.3. The magnetization difference ΔM between up and low branches is proportional to J_c , according to the Bean model in the situation where the H is applied along the film surface ^[2.31]. For the geometry with H applied perpendicular to the film, which is the most important scenario for most of the applications, the modified Bean model ^[2.32] gives

$$J_c = 20\Delta M / [w(1 - w/3l)] \quad (2.12)$$

where w and l is the width and length of the film and M here is the magnetic moment per volume. Fig. 2.4 illustrates the J_c as function of H measured on a same sample using

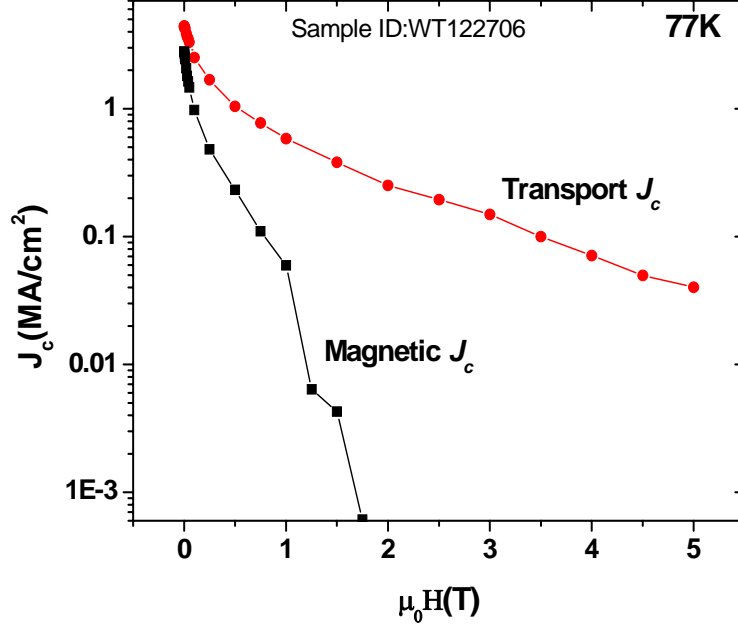


Fig. 2.4: J_c as function of H measured on a same sample using traditional transport (transport J_c) and SQUID magnetization (magnetic J_c).

traditional transport (transport J_c) and SQUID magnetization (magnetic J_c). It can be seen that, even without applying H , the transport J_c is much higher than the magnetic J_c and the ratio between them is about 1.5 at 77 K. This ratio increases to about 10 at 1 Tesla and keeps increasing with H field. One important question immediately following is that which technique gives the J_c closer to the practical situation. Considering the effective thermal conduction in the real device working at 60 to 70 K, larger scale application especially as superconducting magnet requires that the internal power dissipation be less than 10^{-5} - 10^{-6} W/cm³. This corresponds to a criterion E -field in the range of 10^{-3} - 10^{-4} μ V/cm, which is 3-4 orders of magnitude below the typical 1 μ V/cm applied in the

transport measurement. On the other hand, since ΔM changing with H is also due to the flux creep when one characterizes J_c using SQUID magnetometer, it continuously generates an E -field across a sample and the E -field in the perimeter is given by ^[2.33]

$$E(J) \approx \frac{\mu_0 \pi a \tau (dJ/d\tau)}{12} \quad (2.13)$$

which is also proportional to $\tau(dM/d\tau)$ since $dJ/d\tau = dM/d\tau$. This time dependent study, so called magnetic relaxation experiment, has been done using a SQUID-based magnetometer ^[2.34]. Using the typical instrumental settling time of 10-30 seconds, the resulting E -fields were found in the range of $10^{-3} - 10^{-4} \mu\text{V/cm}$. Therefore the SQUID magnetization has been applied as the major J_c characterization technique in my study due to its close resemblance to practical applications.

2.5 The Effect of Applied Magnetic Field on J_c

It is known that the pinning structure is very sensitive to experimental conditions such as growth techniques, growth conditions, substrates and the buffer layer used. Experimentally it is difficult to fabric samples with an exclusive pinning structure and J_c might be determined by the interplay between vortices and multi-scale pinning potential. The situation also depends on the applied magnetic field H . At low H , inter-vortex distance is large and inter-vortex interaction shall be negligible. In this single-vortex (SV) pinning regime, while extrinsic factors such as microstructure degradation and material non-uniformity are absent, J_c is simply determined by the pinning quality of the dominant pinning centers and

$$J_c = cF_p / \Phi_0 \quad (2.14)$$

Note here F_p represents the pinning force per vortex length. The SV pinning regime is indicated by a J_c plateau, as shown in Fig. 2.5 where J_c of a typical YBCO film is plotted as function of H in a log-log scale. The YBCO film is fabricated using PLD and J_c is interpreted from the hysteresis loop using the Bean model. Usually the SV pinning regime only locates within a field range less than a characteristic field B^* , which is only several

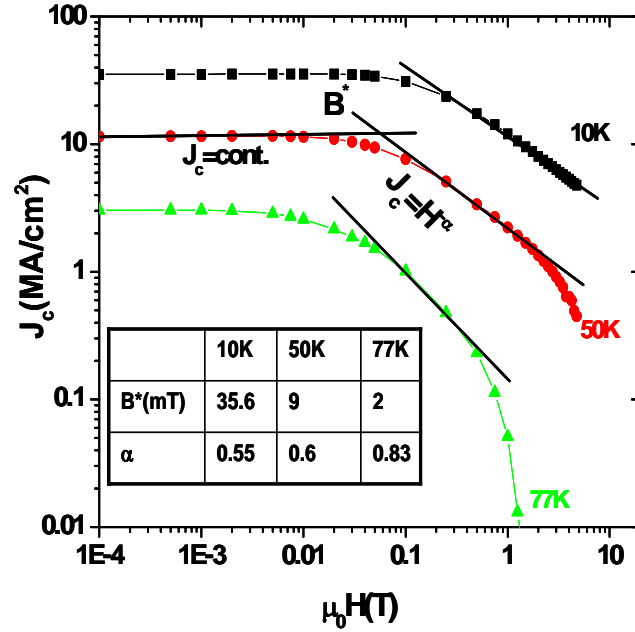


Fig. 2.5: J_c as function of H of a typical YBCO film plotted in a log-log scale and at various temperatures. Inset table gives the characteristic field B^* , which sets the boundary of SV regime, and α value at each given temperature.

to several tens of milliTesla and decreases with increasing temperature. This B^*-T dependence could be qualitatively attributed to the increasing penetration depth λ with temperature since λ defines the range of the interactions between the vortices.

Specifically, for inter-vortex distance $a < \lambda$ the inter-vortex interaction is logarithmic while for large distance $a > \lambda$, it becomes exponentially small^[2.35].

As H increases, both vortex density and the vortex-vortex interaction increase. In this case, not only pin's quality F_p but also density n_p matters. Empirically J_c can be fitted by $J_c \sim H^\alpha$ represented by a line in log-log scale. The smaller the α -value, the better is the in-field J_c performance. Several factor such as temperature, defect structure even characterization technique applied could influence the α -value. The effect of temperature is illustrated in the inset table of Fig. 2.5. It can be seen that higher temperature leads to larger α -value. Qualitatively this can be explained by the pronounced thermal assisted flux motion (TAFM) at higher temperatures. On the other hand, the α -value can be greatly reduced by insertion of stronger pinning centers such as BaZrO₃ (BZO) nano-rod. A 40% reduction in α -value was observed in our group where same deposition and measuring techniques were applied. The power relation $J_c \sim H^\alpha$ also evolves with increasing H and at higher H , a much faster J_c reduction with increasing H is observed as the system approaches to the irreversible field B_{irr} . In addition to the possibility of limited pin's density, a much more enhanced thermal fluctuation could be another reason for this accelerated J_c decay as suggested by the faster drop at 77 K. Further complication involved in the attempts to quantify the J_c - H dependence originates from the different characterization techniques applied in various studies. Despite the difference in J_c values, both the α value and characteristic fields such as B^* and B_{irr} are influenced by characterization technique^[2.34], which is also observed as shown in the Fig. 2.4. However,

qualitatively the H dependence of J_c could be understood as the outcome of interactions between vortices and defects plus the thermal fluctuation.

2.6 The Effect of Temperature on J_c

Comparing to field dependence of J_c , the effect of temperature on J_c is more straightforward. As shown in Fig. 2.6, where the SF J_c is plotted as the function of reduced temperature T/T_c , it monotonically decreases with increasing T . Moreover, $J_c - T$ can be well fitted by the flux creep model $J_c \sim \exp(-T/46.8)$ with R^2 of 0.9948, indicating that TAFM is probably the dominant mechanism of $J_c - T$ [2,36]. Deviations are observed, however, near T_c . This

could be caused by the additional temperature dependence of the carrier density $n_s \sim (1 - T/T_c)$ near T_c , as suggested by G-L theory.

How J_c evolves with magnetic field and temperature is of great importance to the HTS material application,

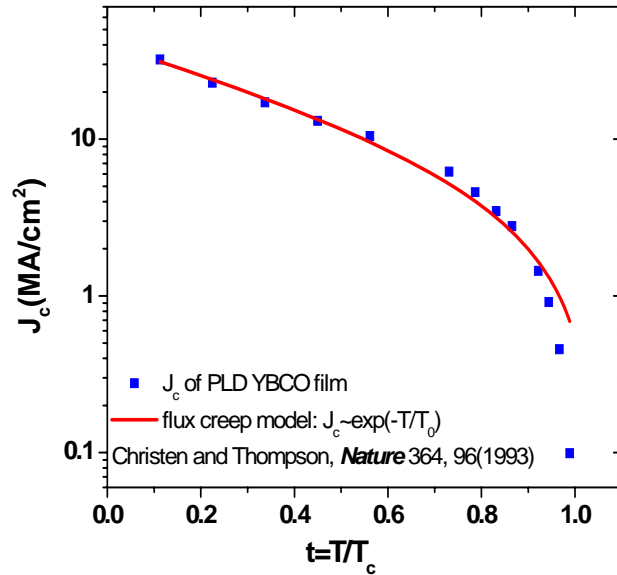


Fig. 2.6: J_c as function of reduced temperature T/T_c measured on a typical YBCO film plotted in a semi-log scale. Solid line represents the flux-creep model predicted $J_c - T$ dependence and T_0 is 46.8 K

especially in the large-scale power-related aspect. Qualitative or at least semi-quantitatively we have understood their effects and the next step would be focused on how to improve the performance of HTS film by defect structure engineering. However, there are still many interesting and also puzzling phenomena that challenge our understanding for both technical development and basic physics in HTS films. This dissertation will be focused on the long-standing issue: thickness dependence of the critical current density in YBCO films.

2.7 Thickness Dependence of J_c in YBCO Film

Aiming at the large critical current carrying capability at a fixed T and H , one of the most important areas in YBCO CC research is to obtain high current carrying capability. Two different distinct routes are: (a) further increasing J_c by optimizing growth conditions; (b) realizing the state-of-art thin-film J_c in a thick film. It seems the former approach is limited by the HTS nature of pronounced thermal creep even for the less anisotropic YBCO. Some researchers have switched gears to the latter route since 1993. Foltyn *et al* reported their experimental results of PLD YBCO films with various thickness (t) on single crystal substrates ^[2,37]. Unfortunately, J_c monotonically decreases with increasing film thickness from 0.2 μm to 1 μm as measured at 77K in SF. Further increasing film thickness up to 6.4 μm has less effect on J_c and J_c saturates at 1MA/cm². Crystalline degradation caused J_c reduction was excluded through X-ray analysis but progressive film discontinuity with increasing thickness was suspected by the authors. As the follow up study, Foltyn *et al* also studied J_c - t dependence of YBCO films deposited

on metal substrates using sequential ion milling^[2.38]. Due to the poor in-plane texture on metal tape, the overall J_c was lower than those on single crystal substrates(see Fig. 2.7). Interestingly, J_c-t behavior was not affected qualitatively by the choice of substrates. Ion milling of two thicker films (3.0 μm and 4.7 μm) and one thinner film (0.68 μm) identified “dead layer”, where no current was carried, on top and bottom of the thicker films while none of them was observed in the thinner one (see Fig. 2.8). They concluded that the top “dead layer” was associated with a distinct microstructural transition at 1 – 2 μm , while the bottom one was related to chemical inter-diffusion across the film/substrate interface.

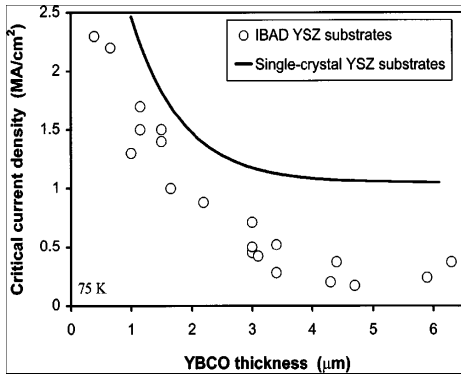


Fig. 2.7(as plotted in Ref. [2.37]):
 J_c-t comparison between YBCO films grown on single crystal substrates and metal tape at 75K and self-field.

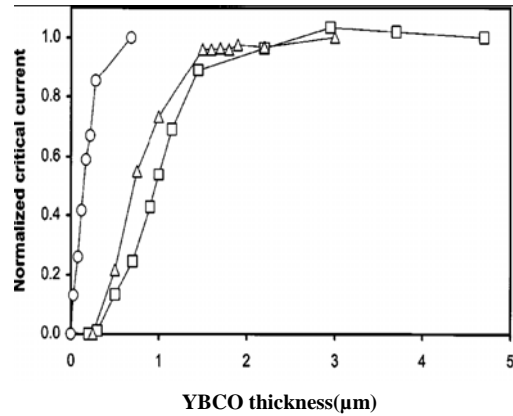


Fig. 2.8 (as plotted in Ref. [2.38]):
Milling generated J_c-d from three CC with thickness of 0.68, 3.0 and 4.7 μm . “Dead layer” is observed for two thick samples.

A comparative study of J_c-t of PLD YBCO films grown on single crystal SrTiO_3 (STO) substrates and metal tape (RABiTS) incorporated with microstructure evolution with thickness was reported by B. W. Kang *et al*^[2.39]. Similar J_c-t was observed for both types of samples except the overall high J_c was observed for YBCO films grown on

single crystal STO. The author concluded that different mechanisms were responsible for J_c-t on different substrates. For YBCO grown on single crystal STO substrates, J_c degradation is attributed to the growth transition to a-axis-oriented(100)($t \geq 0.88\mu\text{m}$) growth as well as the worse in-plane texture, while for YBCO on RABiTS, none of above was observed but a degradation of overall cubic texture as well as increasing porosity with thickness was regarded as the major reason for the suppressed J_c . However, within film thickness from 0.2 to around 0.6 μm where the major J_c reduction occurs, microstructure degradation with changing thickness is almost negligible as illustrated by Fig. 2.9. This important observation was confirmed by the recent reported detail microstructure study on PLD YBCO film on single crystal STO substrates using high-resolution x-ray diffraction and the Rutherford backscattering spectrometry [2.40].

Due to the microstructure degradation identified in thick YBCO film, theoretically it is

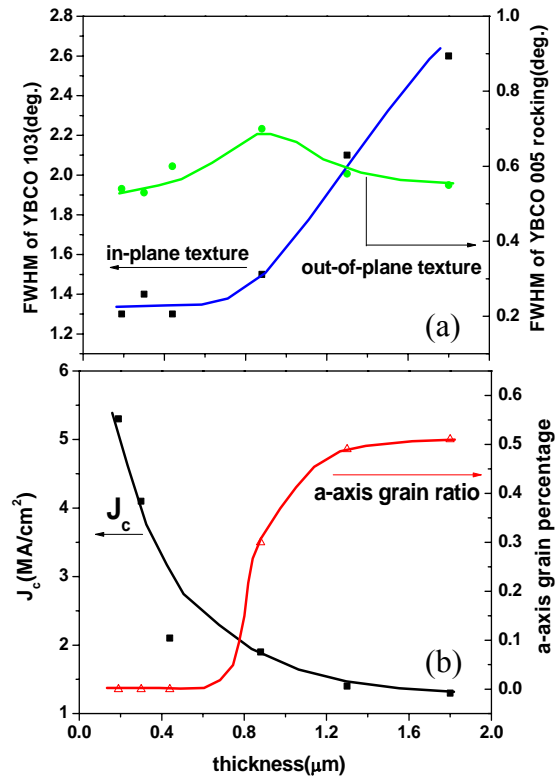


Fig. 2.9(data extracted from Ref. [2.39]): Thickness dependence of (a) in-plane texture and out-of-plane texture; (b) critical current density and portion of a-axis orientated grain in the YBCO films grown on STO single crystal substrate.

possible to slow down or stop this degradation by providing a refurbished growing surface. Experimentally it has been achieved by inserting thin template layer which has near-perfect lattice match to YBCO. Q. X. Jia *et al* fabricated such trilayer structure as YBCO/CeO₂/YBCO [2.41]. Each YBCO layer has thickness $\sim 1.1 \mu\text{m}$ and $J_c \sim 1.4 - 1.5 \text{ MA/cm}^2$. Hence a 60% J_c enhancement was achieved as comparing with a single layer $2.2 \mu\text{m}$ -thick YBCO film using the same growth conditions. Recently Foltyn *et al* expanded the trilayer structure into a multilayer structure [2.42]. In their experiment, six YBCO layers, each $0.55\text{-}\mu\text{m}$ -thick and isolated by $\sim 40 \text{ nm}$ -thick CeO₂ layers were fabricated using PLD, and it was found that J_c of this multilayer preserves the single $0.55\text{-}\mu\text{m}$ -thick film J_c (see Fig. 2.10). It was suggested that the additional five film/substrate interfaces, where a $\sim 20 \text{ nm}$ -thick layer of misfit dislocations locates (see Fig. 2.11), are responsible for the remarkable J_c at such large thickness ($3.35 \mu\text{m}$).

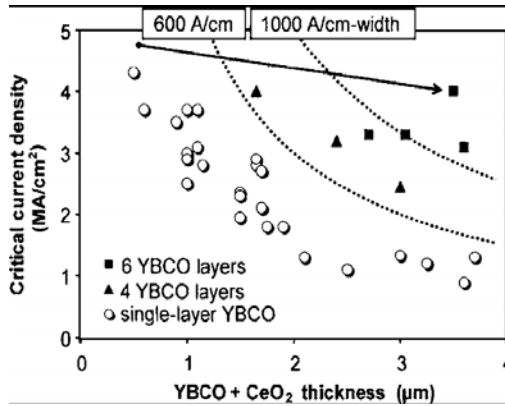


Fig. 2.10(as plotted in ref. [2.42]): J_c as function of thickness for multilayered films (solid), plotted together with data taken on single layer YBCO films (open).

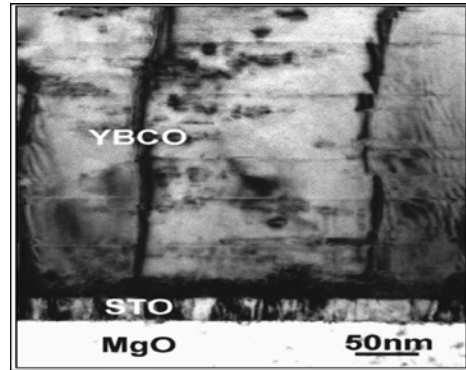


Fig. 2.11(as plotted in ref. [2.42]): Cross-sectional transmission electron microscope image of a YBCO film grown on single crystal MgO substrate. A high density of defects near the YBCO/SrTiO₃ interface regarded as the dominant pinning centers is visible as a dark band.

It should be noticed that J_c-t seems to be independent of growth technique. Similar trend was also observed on films produced by liquid phase epitaxy ^[2.43], chemical-vapor deposition ^[2.44], *ex situ* BaF₂ ^[2.45] and metal-organic deposition processes ^[2.46]. Feldmann *et al* reported an observation of bilayer structure in *ex situ* BaF₂ processed 2.9 μm -thick YBCO film ^[2.45]. The ion-milling generated J_c-d (d refers to remaining thickness), which is shown in Fig. 2.12(a), displays uniform J_c across the entire thickness. However, J_c-d deviates from J_c-t with overall lower J_c . Interestingly, J_c-d of a thinner 2.0- μm -thick film, which is shown in Fig. 2.12(b), seems approaching original J_c-t curve. According to the author, the difference between the milling generated J_c-d and J_c-t measured on as-grown YBCO film could be the result of prolonged growth time, which promoted a higher degree of interfacial degradation. Thus one may speculate that, without microstructure and interfacial degradation, the J_c-d should have followed the sub-linear thickness dependence. The question then arises that whether J_c-t reflects an intrinsic interaction between vortex and surrounding pinning landscape? Knowing that J_c is not only determined by a still *unknown* pinning structure, but also the nature of flux creep, accurate quantification of J_c-t seems necessary.

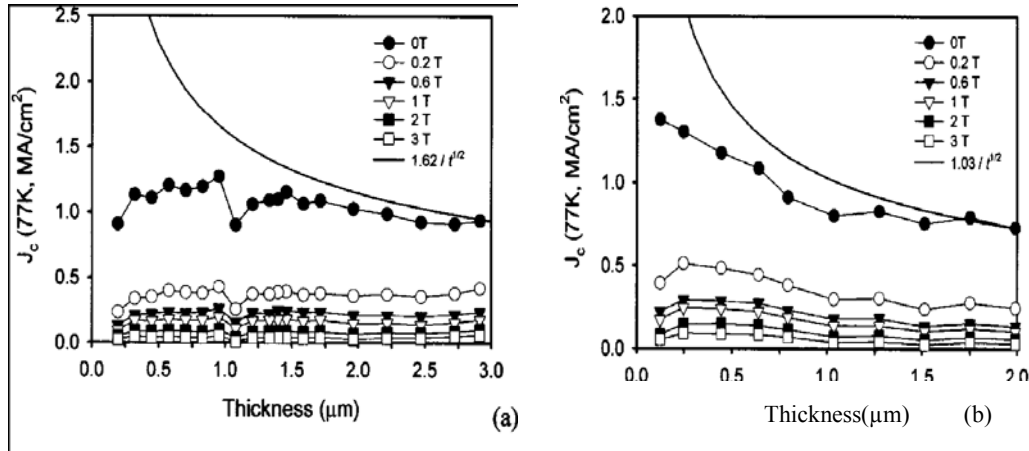


Fig. 2.12(as plotted in ref. [2.45]):
Milling generated J_c - d at 77K and different fields for (a) the 2.9 and (b) 2.0 μm -thick films.
Solid lines are fits to $J_c - t$ from as-deposited samples.

2.8 Weak collective pinning model

Microstructure analysis

indicates that typical PLD YBCO films suffer little microstructural degradation in the thin film regime ($t \leq 0.6\text{-}0.8 \mu\text{m}$). However, major J_c reduction with increasing thickness happens in this thickness regime. Moreover, most of the reported J_c - t data can be fitted by $J_c \propto 1/\sqrt{t}$ as

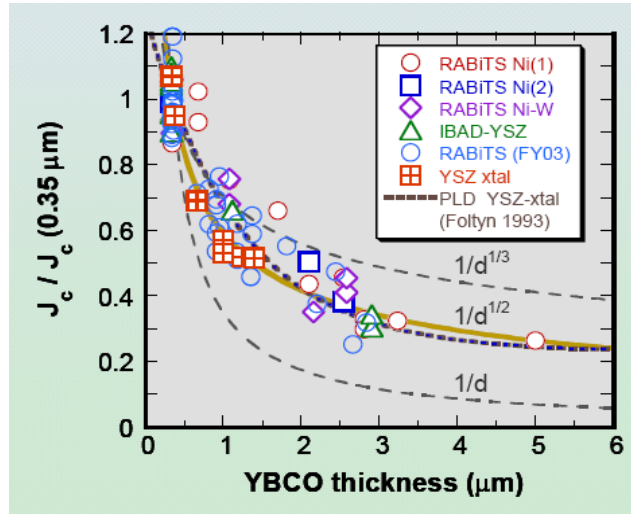


Fig. 2.13(as plotted in ref. [2.47]):
 J_c of as function of thickness measure at 77K and SF reported by different groups in a normalized scale. Most of the data points can be more of less fitted by $1/\sqrt{t}$.

shown by Fig. 2.13 [2.47]. Interestingly, the same thickness dependence has been

predicated by weak collective pinning model proposed by Larkin and Ovchinnikov in 1979^[2.48].

The idea of weak collective pinning can be illustrated in Fig. 2.14, as plotted in ref [2.35], where a single vortex line is subjected to weak randomly-distributed point pinning centers. The total pinning force acting on the vortex line segment of length L is

$$F_p(L) = (f_p^2 n_i r_p^2 L)^{1/2} \quad (2.15)$$

where f_p is the elementary pinning force, n_i is pin's density and r_p is pin's effective radius. The pinning force $F_p(L)$ competes with the Lorentz force $F_L(L) = j \Phi_0 L$, which grows linearly with L , whereas $F_p(L) \propto L^{1/2}$ shows only a sublinear growth due to the random distribution of pinning centers. These dependences give that, at critical state,

$$J_c = (f_p^2 n_i r_p^2 / \Phi_0^2) L^{-1/2} \quad (2.16)$$

which decreases sub-linearly with increasing L (or t). Obviously this square-root dependence should have held in entire thickness range if vortex line was rigid. In fact since the vortex

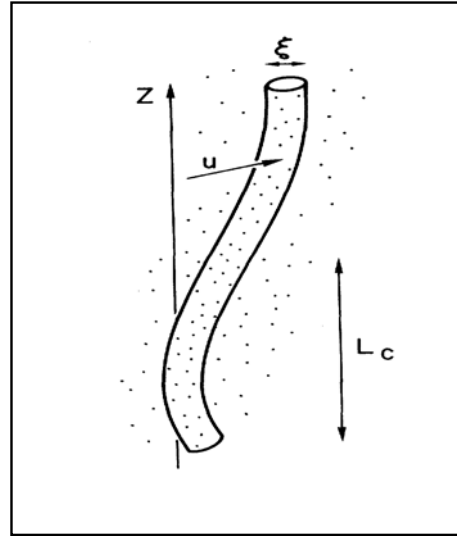


Fig. 2.14(as plotted in ref. [2.35]): Single vortex line is pinned by the collective action of many weak point-like pinning centers. In order to accommodate optimally to the pinning potential, the flux line deforms elastically by L_c , the longitudinal collective pinning length.

line is elastic, it can bend itself in order to find the most favorable position in the random potential. However, such deformation will cost an elastic energy $E_{el} = \varepsilon_l (r_p/L)^2 L$, which in turn competes with the pinning energy $E_p = F_p(L) r_p$ [here $\varepsilon_l \approx \varepsilon_0 = (\Phi_0/4\pi\lambda)^2$ is the vortex

line tension]. At $L > L_c$, where L_c is defined by the equality $E_{el}(L_c) = E_p(L_c)$, the vortex can readjust itself elastically to the optimal local configuration, consequently the $F_p(L)$ grows linearly with increasing L and the square-root dependence $J_c \propto 1/\sqrt{L}$ is cut off. The vortex then breaks into segments with length of L_c , each of which is pinned independently and competes as one unit with the Lorentz force $F_L(L_c) = j\Phi_0 L_c$. $L_c = (\epsilon_0^2 / f_p^2 n_i)^{1/3}$ is called the correlated pinning length or Larkin length. Since f_p is not directly accessible in an experiment, the ratio J_c/J_0 is typically used as the fundamental quantity characterizing the strength of pinning potential and Larkin length can be expressed in a simple form as $L_c \approx r_p(J_0/J_c)^{1/2}$.

With the assumption that random distributed point-like defects determine the J_c in YBCO films, it is plausible to apply the weak collective pinning model to describe the vortex behavior in PLD YBCO films. Considering a superconducting film at weak field where vortex-vortex interaction is negligible, J_c as function of thickness can be described with the weak CP model as:

$$J_c \propto 1/\sqrt{t} \quad (t < L_c, \text{ 2D collective pinning regime})$$

$$J_c = J_{c0} \quad (t \gg L_c, \text{ 3D bulk pinning regime})$$

where J_{c0} is the bulk current density only depends on T and H . However, the L_c given by the weak CP model is much smaller than that of the thickness range where J_c-t occurs. For example, taking typical J_c of 4MA/cm² for YBCO film and J_0 of 36MA/cm² at 77K and SF, the L_c is found to be 4.5 nm. It should be realized that YBCO film represents a strong pinning system in which the J_c/J_0 ratio is one to two orders of magnitude higher than that of weak pinning system such as YBCO single crystal. This raises a question

whether the result of weak CP model can be directly applied on strong pinning system without any modification.

2.9 Summary

The most attractive nature of HTS material is their ability to carry large current with very minimal dissipation. Their current carrying capability is influenced by both temperature and applied magnetic field, owing to the dissipative nature of flux motions induced by both TAFM and Lorentz-type driving force. J_c responses to a changing temperature and magnetic field can be understood as a result of flux dynamics even without knowing the detail pinning structure. However, regarding the thickness dependence of critical current density, even though it quantitatively follows the collective pinning behavior at 77 K and SF, it occurs in a thickness range far beyond the predicted one. This discrepancy may arise from the different pinning environment in film and crystal, and necessitate modifications of the original weak pinning CP theory. On the other hand, since thermal fluctuation also plays an important role and most of the reported J_c-t data is only at 77 K and SF, it is also important to expand the investigation scope to a larger temperature and field region. This will serve the purpose of further quantifying J_c-t and providing the insight into the underlying mechanism.

CHAPTER 3: The Effect of Temperature and Magnetic Field on Thickness Dependence of Critical Current Density

3.1 The Effect of Temperature on J_c - t

YBCO films were fabricated on single crystal (100) LaAlO_3 (LAO) substrates using pulse laser deposition (PLD) technique. The laser energy density on the target was $\sim 3.2 \text{ J/cm}^2$ and the repetition rate was 10 Hz. The deposition was carried out onto substrates heated to 765°C at 230 mTorr oxygen followed by the oxygen annealing in 360 Torr O_2 for 50 minutes^[3.1]. About 24 films were fabricated with variable thicknesses ranging from 0.01 to $0.7 \mu\text{m}$ to assure reproducibility. The thickness was calibrated with Tencor P16 profiler. The superconducting properties of the samples were characterized using a Quantum Design SQUID magnetometer. The superconducting transition temperature (T_c) of the samples was obtained from zero-field-cooled (ZFC) magnetization (M) as function of T and the J_c was interpreted from sample's hysteresis M - H loop using the Bean model^[3.2].

Most of the films thicker than $0.05 \mu\text{m}$ have the magnetically measured J_c values greater than 2 MA/cm^2 at 77K and SF. Note that the magnetic J_c at SF and 77 K interpreted from the irreversible magnetization is usually 1.5~2 times lower than that from the transport measurement^[3.3]. This means that the quality of the samples used for this experiment is comparable to that of standard high-quality YBCO films. However, the

superconductivity degrades dramatically when t decreases to less than $0.05\text{ }\mu\text{m}$. Since the defect structure strongly depends on the substrate termination, especially at the early stage of epitaxy, this degradation is most probably associated with atomic disorder (cation and ionic disorder) near the film/substrate interface. However, with increasing t beyond certain critical thickness t_c , the epitaxial stress (or strain) will be relieved accompanying with the appearance of structural defects. In particular, this critical thickness t_c up to which the film remains under epitaxial stress or strain depends on the substrate termination. The reported t_c is usually between 0.015 to $0.06\text{ }\mu\text{m}$ depending on the substrate used ^[3.4]. In our study, since the mismatch between YBCO film and LAO substrate is $\sim 2.6\%$ which is comparable to 2.1% on SrTiO_3 ^[3.5], this critical thickness is estimated to be $\sim 0.06\text{ }\mu\text{m}$.

The Zero-Field-Cooled (ZFC) M - T measurement results on seven samples of various thicknesses are shown in Figure 3.1. The applied H field is 10 Oe along the c -axis of the film. The magnetic moment M is normalized to its absolute value at 10 K to eliminate the effect of sample to sample difference in demagnetization factors.

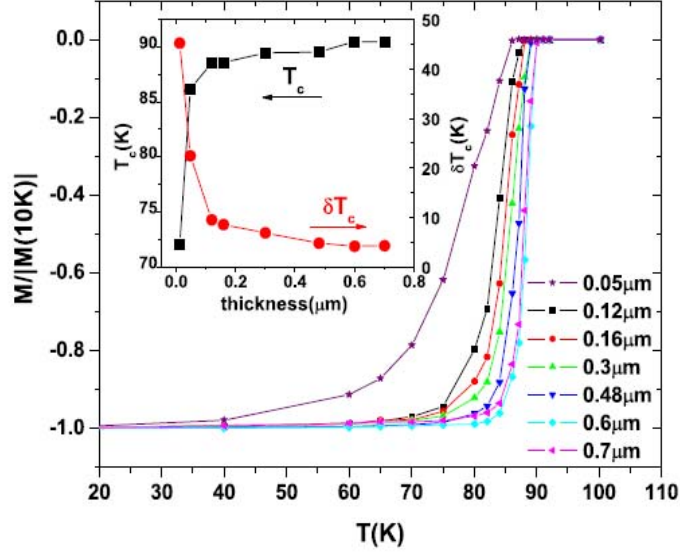


Fig. 3.1: Shown is normalized $M [M/M(10K)]$ as function of T for YBCO films with various thickness. Shown in the inset are the T_c and δT_c as function of thickness

A systematic decrease of T_c as well as increase of the transition width δT_c (10% - 90%) can be observed with decreasing sample thickness and the details are illustrated in the inset of Figure 3.1. For example, for the 0.6 μm-thick sample, T_c is 90.5 K while for the 0.05 μm-thick sample, it drops to 86.2 K. Meanwhile the δT_c decreases from 22.5 K at 0.05 μm to 4.2 K at 0.6 μm. T_c and δT_c experience a much dramatic degradation as t further decreases below 0.05 μm, indicating the dominant role of disorder when t reduces below t_c . Especially at ~ 0.01 μm, nearly no hysteresis is observed in the $M-H$ loop at any T above 50 K and its T_c and δT_c are 72 K and 45.2 K, respectively (see the inset of Figure 3.1). Hence it can be literally considered as a “dead” layer carrying no J_c in the temperature range at and above 50 K. To minimize the complication from the material non-uniformity associated with disordered layer across the thickness, the effective thickness (0.01 μm less than the actual thickness) was applied to calculate the J_c .

Although the material non-uniformity occurs only in very thin films range below 0.05 μm , a gradual increase of T_c and decrease of δT_c can be still observed in Fig.3.1. As film thickness exceeds 0.6 μm , both T_c and δT_c saturate around that of 0.6 μm -thick films. Due to the remarkable similarity in the increased δT_c by increasing H field in $M-T$ curves^[3.6] as well as in resistivity $\rho-T$ curves,^[3.7] we argue that the transition broadening shown in Fig. 3.1 is most probably caused by the lower activation energy against thermally activated flux motion (TAFM) associated with shorter vortices in thinner films.

Fig.3.2(a) depicts the SF J_c-t curves at various temperatures in the range of 50 K to 88 K, which covers the temperatures of interest to most HTS applications. The semi-log scale is employed to magnify the curve at elevated temperatures. Solid lines are drawn for eye guidance and error bars correspond to the average over the two samples with same thickness. It is clearly shown that the monotonic decreasing J_c-t observed at 77 K reported earlier only sustains in the thickness range $> 0.1 \mu\text{m}$ at $T < 84$ K. When normalized to the J_c value of the 0.6 μm -thick film, as shown in Figure 3.2(b), the reduced J_c^r at various T in Figure 3.2(a) diverges in the thinner regime ($t < 0.3 \mu\text{m}$) while they almost coincide when $t \geq 0.3 \mu\text{m}$ (thicker regime) at T near and below 84 K. However, with further increasing T , even J_c-t in thicker regime deviates from the main trend and continuously weakens as T approaches T_c . This means that the effect of T on the SF J_c-t is negligible in thicker regime while thermal fluctuation is not a concern. The coincided part of the J_c^r-t curves can be well fitted with $J_c \propto t^{-1/2}$ (dotted line). In the thinner regime, systematic deviation of the J_c-t curves from the $t^{-1/2}$ fitting is observed from Fig .3.2(b). The deviation increases with T , suggesting that it is related to the more

intensified TAFM at higher temperatures which significantly reduces J_c . In addition, the deviation is more serious at smaller t , resulting in a broad J_c peak at thickness t_m . t_m is about 0.1 μm at 77 K and increases with T since the TAFM affected thickness range expands with increasing T . When T increases to 84 K, the J_c peak shifts to a larger $t_m \sim 0.3 \mu\text{m}$. Meanwhile, the t at which the $J_c - t$ curves deviates from $J_c \propto t^{-1/2}$ also increases with temperature. As T approaches T_c , the TAFM effect becomes overwhelming, resulting in the $J - t$ curve deviating from $J_c \propto t^{-1/2}$ in almost entire thickness range in Figure 3.2(b). At 88K, the monotonic decreasing $J_c - t$ is reversed to monotonic increasing.

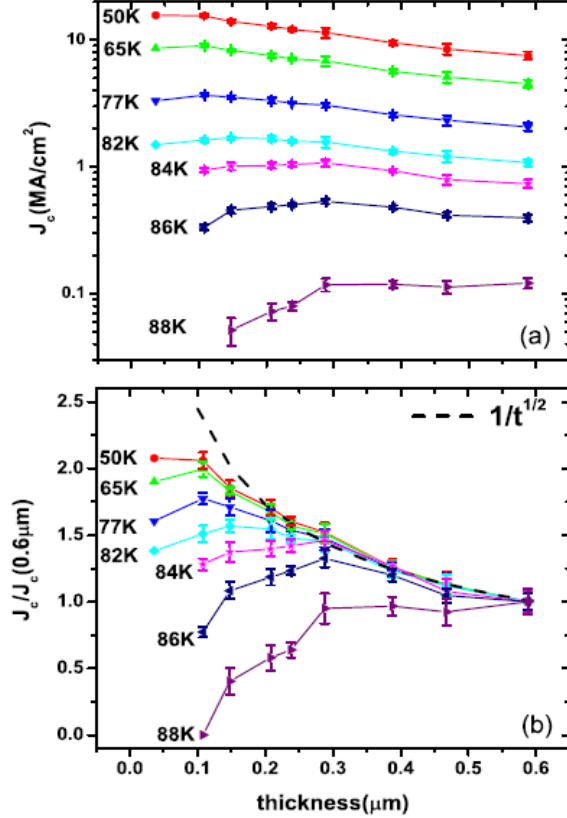


Fig. 3.2: Shown is (a) $J_c(SF) - t$ at various temperatures. The error bar corresponds to the average over different sets of samples with same thickness. (b) The reduced $J_c^r = J_c/J_c(0.6\mu\text{m})$ as function of thickness at various temperatures. The dashed line represents the fitting of $1/t^{1/2}$.

Note that the T effect on t_m is more pronounced at elevated T above 77 K, which is consistent with a weak [3.8] or even no T dependence of t_m

[3.9] observed at $T \leq 77$ K by other groups. This thickness effect seems to be inherently determined by the lower activation energy associated with thinner films, which is

confirmed by the observation of considerable increase of relaxation rate dM/dt in the thinner YBCO films at $T \geq 70$ K ^[3.10].

3.2 The Effect of Applied magnet field on $J_c - t$

If the deviation of $J_c - t$ from the $J_c \propto t^{1/2}$ curve is caused mainly by TAFM, much enhanced effect is expected in the applied H which further facilitates TAFM. Therefore a J_c crossover is expected if one plots J_c as function of H of films with various thicknesses at certain T . Previous experiments on single layer YBCO ^[3.11] as well as HTS superlattice ^[3.12] did observe such crossover. In our study, this crossover could be also inferred as summarizing $J_c^r - t$ curves at various H measured at 77 K and 50 K in Figures 3.3(a) and 3.3(b), respectively. The H field causes $J_c^r - t$ to deviate from the $J_c \propto t^{1/2}$ curve in the thinner film

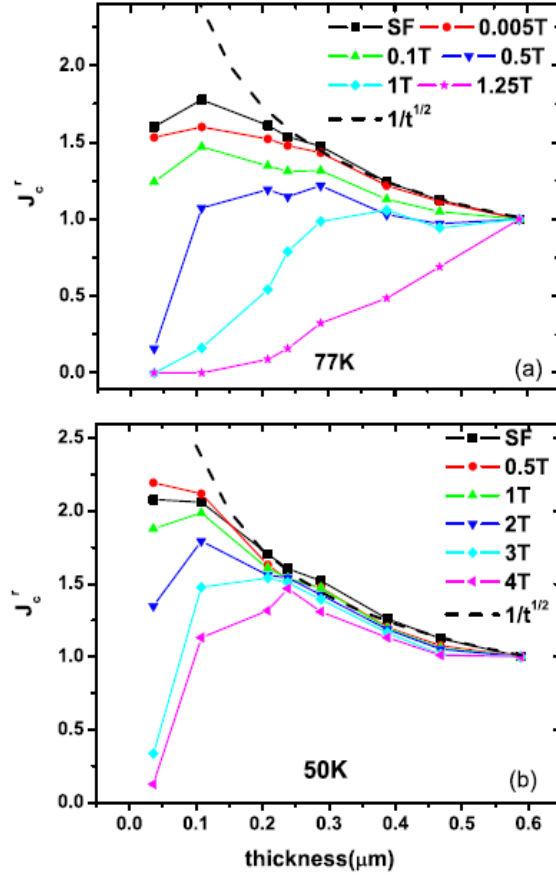


Fig. 3.3: Shown are $J_c^r - t$ curves at (a) 77K and (b) 50K, respectively, at various H fields. The dashed line represents the fitting of $1/t^{1/2}$.

regime first at low H and the thickness range affected increases with H at a given T . Moreover, J_c at smaller thickness of the curve drops much more than that at the thicker part. Consequently a broad J_c peak similar to that on the SF $J_c^r - t$ curve appears with increasing H which is followed by a complete reversal of the $J_c^r - t$ curve from monotonic decreasing to monotonic increasing at higher H if T is high enough. This entire sequence can be clearly seen in Figure 3.3(a) at 77 K and the reversal occurs at ~ 1.25 Tesla. The similar trend has also been observed at lower temperatures despite some quantitative differences. Basically, higher H field is necessary to generate the same or similar effect on the $J_c^r - t$ curve at lower temperatures. For example, at $T = 50$ K, which is shown in Figure 3.3(b), the broad J_c peak is not fully formed until H increases to 3.0 Tesla, and a complete reversal from monotonic decreasing to monotonic increasing is not realized even at 4.0 Tesla. Instead, a cusp is formed at $t_m \sim 0.25 \mu\text{m}$, which separates the monotonic increasing $J_c - t$ below t_m and the monotonic decreasing $J_c - t$ above it.

3.3 Theoretical Analysis of $J_c - t$

If one compares the T effect with H effect on $J_c - t$, it is interesting to see that both T and H influence $J_c - t$ in a very similar way, or say, through a thermal activated process. Actually the thermal effect on $J_c - t$ has been treated theoretically using the dynamic approach within the frame of original CP model ^[3.13]. In the flux creep region $J < J_c$, since the small induced electric field E is mostly determined by the thermally activated vortex jumps between pinning centers in the direction of Lorentz force F_L , the

thermally activated dynamics of vortices can be described using the E – J characteristics with the form

$$\epsilon = \theta(1 - e^{-\pi\beta_r/\theta}) / t_r \int_0^\pi e^{-\alpha\beta_r/\theta} I_0\left[\frac{f(t_r)\sin\alpha}{\theta}\right] d\alpha \quad (3.1)$$

where $\epsilon = E/\rho_F J_0$, $\beta = J/J_{c0}$, $t_r = t/L_c$, and $f(t) = F_P(t)/F_P(L_c)$ are the dimensionless electric field, current density, film thickness and pinning force line density, respectively, $\rho_F = \rho_n H/H_{c2}$ is the flux flow resistivity and $I_0(x)$ is a modified Bessel function. The strength of thermal fluctuation strength is quantified using a dimensionless temperature θ :

$$\theta = \pi k_B c T / J_{c0} \Phi_0 L_c l \quad (3.2)$$

It can be seen that, besides temperature T , applying magnetic field H also influences θ through 3D bulk $J_{c0}(T, H)$. θ can be also affected by material dimensionality through L_c as well as the defect structure from the average inter-defect spacing l . For some typical YBCO thin film parameters, J_{c0} (77K, SF) = 1MA/cm², $L_c = 0.5 \mu\text{m}$, $l = 50 \text{ nm}$ and $T = 77 \text{ K}$, Eq.(3.2) yields $\theta \approx 6.7 \times 10^{-3}$.

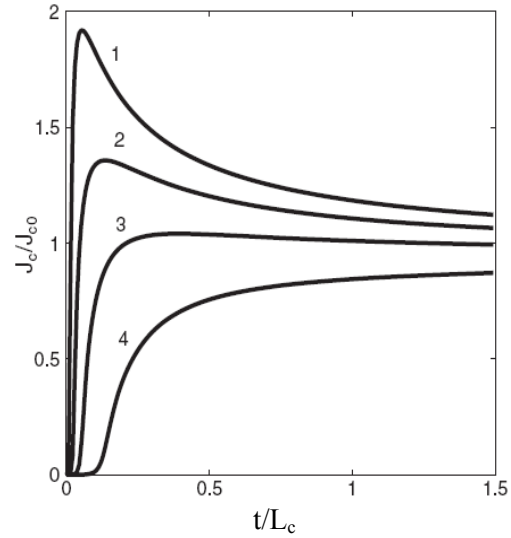


Fig. 3.4 (as plotted in ref. [3.13]): Evolution of the J_c – t described by Eq.(3.2) for different values of (1) $\theta = 0.0065$, (2) 0.01, (3) 0.015, and (4) 0.025.

For a given electric field criteria ϵ_c , the J_c as function of thickness is determined by the implicit Eq.(3.1) with the account of TAFM. Shown in Fig. 3.4 is the evolution of $J_c - t$ with changing θ . $J_c(t)$ is calculated from Eq.(3.1) using $\epsilon_c = 10^{-6}$ for typical E standard of $1\mu\text{V}/\text{cm}$ and $f(t)=[t(1+t)]^{1/2}$, $H/H_{c2}=0.01$ and $\rho_n=0.1\text{m}\Omega\cdot\text{cm}$. It can be seen that, qualitatively, $J_c - t$ calculated evolves with increasing θ in a very similar way as the experimentally observed $J_c - t$ under the influence of changing T and H . In fact, quantitatively this model also fits the experiment data well with R^2 of 0.9154 as seen in Fig. 3.5, where the measured (squares) and calculated $J_c - t$ (blue line) at 65K and 1T are plotted together.

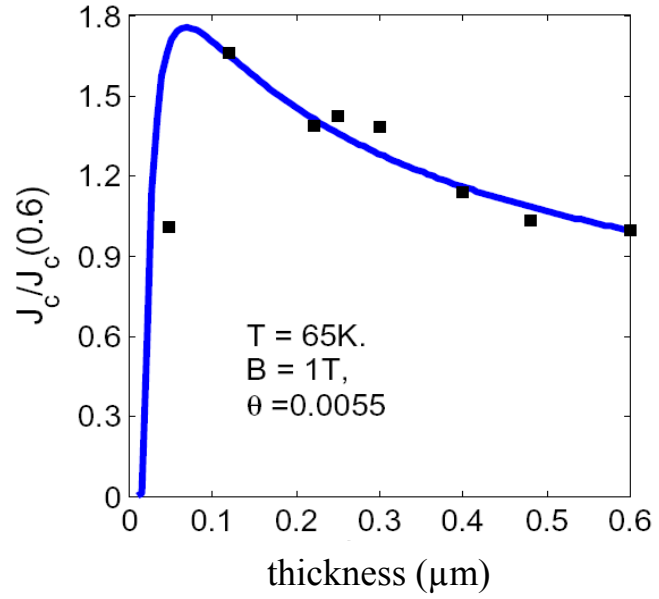


Fig. 3.5: $J_c(t)$ measured (squares) at 65K and 1T and calculated (blue line) from Eq.(3.1).

This remarkable consistency between theory and experiment suggests that $J_c - t$ actually reflects the interplay between TAFM and CP behavior. In order to extract the pure CP behavior, one can drop T very close to zero to suppress the TAFM. Indeed, the $J_c^r - t$ at SF and 10 K (see squares in Fig. 3.6) shows consistency with the CP model in most thickness range down to $\sim 0.2\mu\text{m}$. At $t < 0.2\mu\text{m}$, although monotonic decreasing $J_c - t$ is observed, substantial discrepancy remains. It should be mentioned that the J_c presented in this work is interpreted from remnant magnetization

using the Bean model. In the thin film geometry, the calculated J_c at small H may deviate from real J_c if film thickness is comparable or less than λ_{ab} (λ_{ab} is about 200 nm at 10 K). To ensure a uniform critical state across the whole sample, the $J_c^r - t$ curve was measured at 1.0 Tesla and included also in Figure 3.6. Much improved agreement between experiment and the CP model is observed in the entire thickness range except some minor deviation at $t < \lambda_{ab}$. The mechanism responsible for this minor deviation may be attributed to the material non-uniformity occurred at $t < 50$ nm, which may not be removed completely with the 10 nm-dead-layer correction. Some other unknown mechanism may exist also. Nevertheless, the overall result suggests that the CP model plays a dominant role in the $J_c - t$ behavior of uniform HTS films when TAFM effect is suppressed.

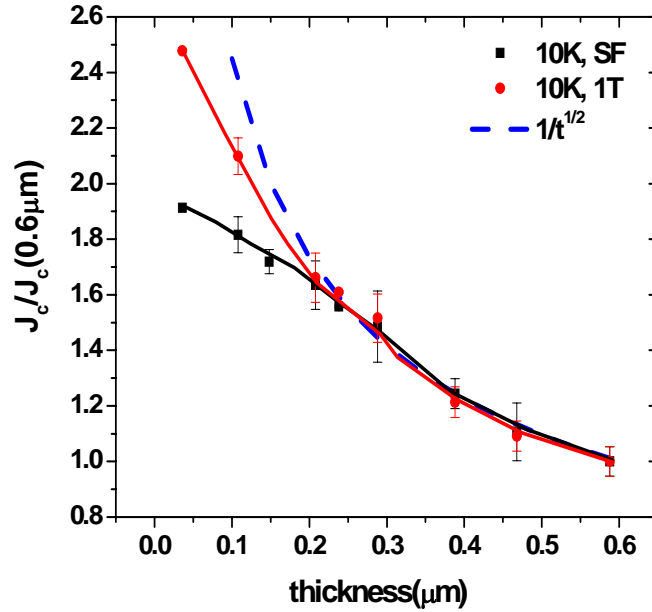


Fig. 3.6: $J_c^r(10\text{K}) - t$ curves at SF and 1.0 Tesla, respectively. The dashed line represents the fitting of $1/t^{1/2}$.

3.4 Conclusions

Even though there is still argument regarding the mechanism behind J_c-t , at least most of the HTS community agrees that J_c-t is the consequence of vortex dynamics and it has little correlation with microstructural evolution with thickness, especially at t less than 0.6-0.8 μm . Although the CP model fits the J_c-t very well after modification, some questions remain. The first question is about the order of magnitude of the Larkin length L_c . In a weak pinning system where J_c is at least two orders of magnitude lower than J_0 , pinning is most likely dominated by point defects like oxygen vacancies with atomic size and r_p is on the order of the coherent length ξ . For anisotropic YBCO, ξ_c is ~ 0.4 nm at 77 K. Consequently L_c is ~ 4 nm, more than two orders of magnitude smaller than the HTS film thickness range at which the J_c-t behavior occurs. In fact, YBCO thin film is a strong pinning system and the typical J_c is $\sim 10\%$ of J_0 at 77 K and SF. This means that atomic size point defects such as oxygen vacancies are unlikely the dominant pinning centers and r_p should be comparable to the dimension of other defects, such as precipitates and secondary-phase inclusions which are on the order of few to tens of nm in dimension ^[3.14-3.16]. Assuming pinning in YBCO films is dominated by these large point defects, L_c would be up to tens of nm, still an order of magnitude smaller than the relevant film thickness at which J_c-t is important. On the other hand, experiment results suggest that a larger L_c exist in YBCO film. For example, the thickness dependence of irreversible field B_{irr} indicated that an extremely long L_c on the order of sub-micrometer in YBCO thin films ^[3.17]. This then raises a question on whether the summation approach originated from the large number of small-size weak pins can still be applied to the case

of sparse large-size strong pins. Considering the strong pinning nature as well as the dispersive nature of vortex line tension in anisotropic HTS material, Gurevich reformulated the weak collective pinning model to account for the multi-scale pinning potential in YBCO films and theoretically demonstrated that the L_c in YBCO films could be as long as $1\text{ }\mu\text{m}$ ^[3,18].

We have found that within the thickness comparable to the modified Larkin length, the $J_c - t$ behavior can be well described by collective pinning model which predicts $J_c \propto t^{1/2}$, in combination with the TAFM effect. Deviation from the CP model occurs when thermally activated flux motion becomes significant at elevated temperatures and applied magnetic fields in the thickness range of $t \leq \lambda_{ab}$. A clear demonstration of the CP model is obtained at 10 K when the TAFM is greatly suppressed. This study of T and H effect on $J_c - t$ suggests that the monotonic decreasing $J_c - t$ in YBCO films is an intrinsic property which reflects the random pinning nature in typical YBCO films. Hence, the $J_c - t$ may be removed either by reducing the L_c via multilayer structure or changing the pinning structure via introduction of strong linear pinning centers.

CHAPTER 4: J_c - t Elimination Using Multilayer Approach

We have studied temperature and magnetic field effect on J_c - t of YBCO films. The remarkable consistency between experimental observation and modified CP theory indicates that J_c - t is most likely determined by the sub-linear thickness dependence of pinning force line density F_p . This sub-linear dependence in turn reflects the random pinning nature of typical as-grown YBCO films. Therefore the key point to eliminate J_c - t is to maintain a constant F_p at various thicknesses. This can be realized by altering either vortex structure or pinning structure. In this chapter we will discuss the approach to eliminate J_c - t using a trilayer structure YBCO/insulator/YBCO.

4.1 Single Vortex in S/N/S Trilayer

Considering a single vortex that is collectively pinned by a random pinning potential, if the vortex length is less than L_c , the vortex stays straight and any local bending to accommodate nearby pinning centers is not energetically favored. Therefore the F_p decreases with increasing thickness as $t^{1/2}$. In order to get rid of this thickness dependence, a scheme that enables the local bending of vortex is the key. One strategy is to “chop” a vortex into two or more segments with construction of (HTS/insulation/HTS)_n multilayer structure. Since it softens the vortex and reduces the cost of elastic energy, the multilayer structure enables the local vortex bending even though the effective vortex length is still within the L_c .

With construction of a superconductor/insulator/superconductor trilayer structure, the so called Giaever transformer, early studies indicate that vortices in two superconducting layers are coupled through magnetic interaction. The original transformer using LTS showed that dissipation in type II superconductor (SC) arises from the motion of the vortex. In his pioneering work, Giaever used two SC tin layers sandwiching a thin insulating SiO₂ layer which electrically isolates the two SC layers^[4.1]. As a dc current passed through one of the tin layers (primary) became large enough to create a flux flow, the voltage drop was observed on both films. This observation presented strong evidence of vortex as an axially coherent entity.

Theoretical calculations based on the Pearl model^[4.2] show that the magnetic coupling force (F_c) is determined on seven characteristic lengths: t_p , t_s , t_i , λ_p , λ_s , ξ_p and ξ_s when inter-vortex interaction is negligible.³³ These correspond, respectively, to the thickness of the primary, secondary SC and the insulating layers, the penetration depth of the primary and secondary superconducting films (λ_p , λ_s), and the coherent length of the primary and secondary films (ξ_p , ξ_s). The maximum coupling force F_{cm} exerted by the primary vortex segment upon a secondary segment is then given by^[4.3]

$$F_{cm} = \frac{\Phi_0^2}{8\pi^2 \rho_{eff}^2} \tilde{F}_{cm} \quad (4.1)$$

where ρ_{eff} is an effective screening radius given by

$$\rho_{eff} = t_i + \lambda_p \coth(t_p / \lambda_p) + \lambda_s \coth(t_s / \lambda_s) \quad (4.2)$$

Except at high fields, \tilde{F}_{cm} is simply a dimension-less quantity of order unity for all values of t_p , t_s , t_l , λ_p , λ_s , ξ_p and ξ_s . Thus at reasonably low fields the magnitude of the F_{cm} is dominated by the prefactor $\Phi_0^2 / 8\pi^2 \rho_{eff}^2$.

4.2 Decoupling Vortex in YBCO/CeO₂/YBCO Trilayer

Now return to the YBCO/CeO₂/YBCO trilayer, to simplify the situation, the thickness of the two YBCO layers is fixed while the thickness of the insulator (t_l) is systematically altered. Qualitatively it is obvious that the inter-vortex segment coupling decreases with increasing t_l . Due to the weakened coupling, the vortex segment in each YBCO layer becomes relatively free to adjust itself to nearby pinning potential. Therefore the system obtains improved pinning efficiency so as J_c . Taking YBCO sub-layer thickness fixed at either 0.25 or 0.5 μm , F_{cm} is calculated using Eq.(4.1) and plotted as function of t_l in a normalized scale $[F_{cm}/F_{cm}(t_l=0)]$ as shown in Fig. 4.1. It is

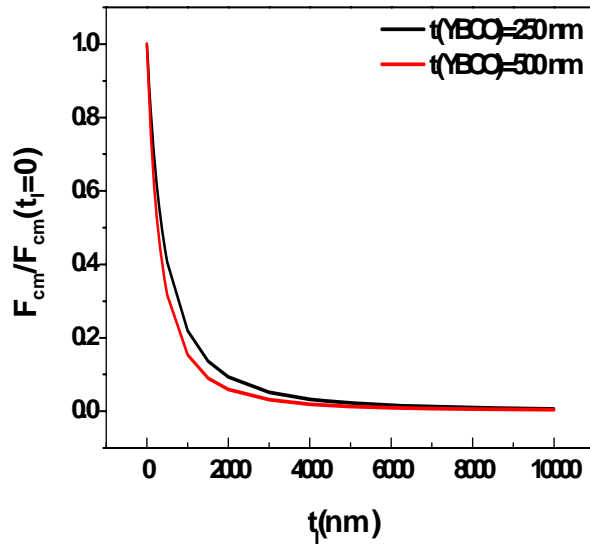


Fig. 4.1: Magnetic coupling force F_c as function of insulator layer thickness t_l calculated from Eq. 4.1. The superconducting layer thickness is fixed either at 0.25 or 0.5 μm .

clear that F_{cm} decreases monotonically with t_I and when $t_I \sim 6.5\lambda_{ab}$, it drops by an order of magnitude. This motivates us to investigate the effect of interlayer magnetic coupling on J_c of trilayered YBCO/Insulator/YBCO films in two different extremes: one is at $t_I \gg 6.5\lambda_{ab}$ where F_{cm} is negligible and the other, at $t_I \ll 6.5\lambda_{ab}$ where F_{cm} is important.

A double-sided YBCO film is an ideal system of negligible F_{cm} because the substrate thickness $t_I = 500 \mu\text{m} \gg 6.5\lambda_{ab}$. The two YBCO films, each $0.5 \mu\text{m}$ thick, were grown on the double-side polished single crystal (100) LaAlO_3 (LAO) substrate. The superconducting properties of the samples were characterized using a Quantum Design SQUID magnetometer and J_c was estimated from the magnetization M-H loops using the Bean model.^[16] First, the J_c of

the double-sided YBCO sample (J_c^{double}) was measured. One YBCO film was then removed using 0.05% nitric acid and the sample's J_c (J_c^{single}) was re-measured. A comparison of the J_c vs. H curves for this sample before and after the etching is depicted in Fig. 4.2 at several different temperatures. Indeed, the J_c^{single} coincides completely

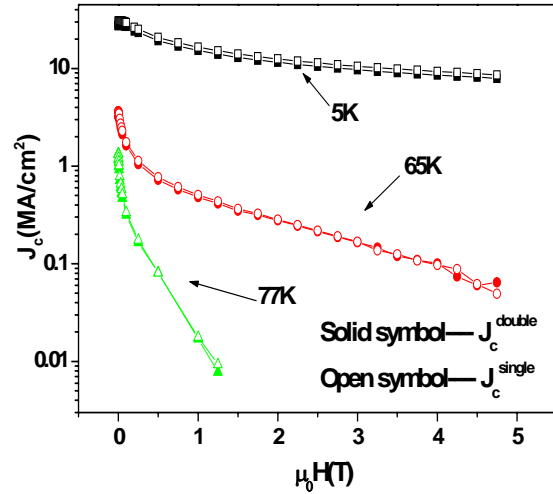


Fig. 4.2: J_c as function of applied magnetic field for a double sided YBCO film ($0.5 \mu\text{m}$ -thick for each side) and its one side after etching of the other.

with the J_c^{double} in the H range of 0 to 5 Tesla and T range of 5 to 77 K. This result suggests no J_c -thickness dependence in a tri-layered HTS system when the two superconductor layers are completely decoupled.

We have also studied the J_c in the trilayered samples in which the two YBCO layers of 0.25 μm thick each were separated by a thin insulating CeO_2 of thickness (t_l) in the range of 0-20 nm. The CeO_2 layer was grown *in situ* with the YBCO layers by switching the YBCO and CeO_2 targets during pulsed laser deposition at 760 °C and 230 mTorr oxygen. Scanning electron microscopy (SEM) and conductive atomic force microscopy (AFM) were applied to analyze the surface morphology and continuity of the CeO_2 layer on the bottom YBCO. Fig. 4.3(a) depicts the SEM micrograph of a 20 nm thick CeO_2 layer grown on a 0.25 μm thick YBCO layer, which suggests a continuous coverage of the CeO_2 layer with some particulates. The conductive AFM image [Fig. 4.3(b)] confirmed that this layer was indeed insulating (dark area) with few conductive

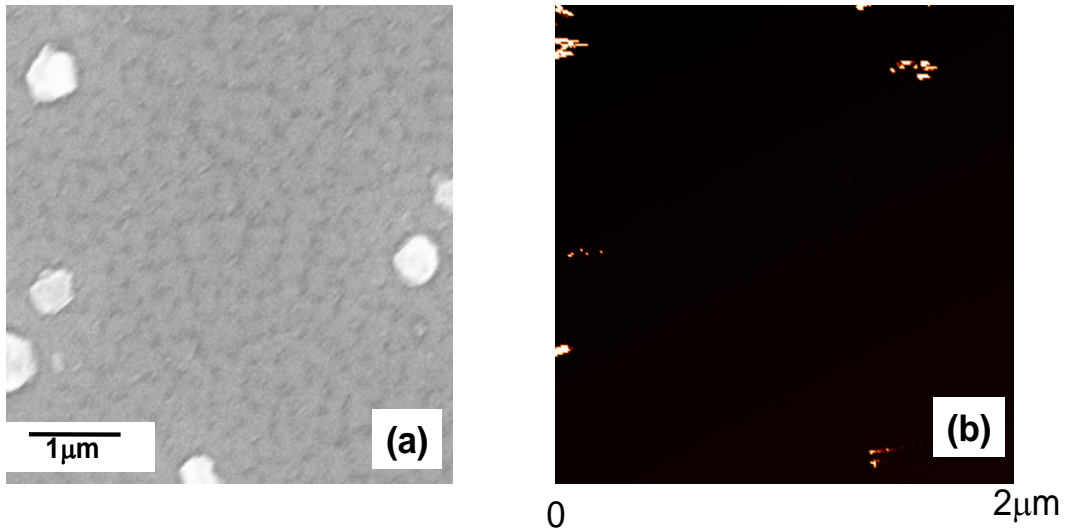


Fig. 4.3: (a) SEM and (b) conductive AFM images of a representative 0.25 μm thick YBCO film covered by 20 nm thick CeO_2 layer.

pinholes (bright spots). At smaller CeO_2 thickness, a slightly higher population of pinholes was observed. For example, on 10 nm thick CeO_2 , the area covered by pinholes increased to 10-12 % as opposed to 1-2% at 20 nm thick CeO_2 . The two superconducting layers are therefore not completely decoupled electrically, which is consistent with the previous report on the attempt to fabricate S-I-S junctions ^[4.4].

Fig. 4.4 shows the J_c value of the trilayered film as function of t_I at 77 K and SF. At $t_I=0$, the J_c value is for a 0.5 μm thick single-layered YBCO film. With increasing t_I , a monotonic J_c increase has been observed. At $t_I=20$ nm the J_c in the trilayered film saturated to the value of the 0.25 μm thick YBCO film (dash-dot line). Since all these trilayered samples have the same effective superconducting cross-sectional area for J_c , the increase of the J_c with the thickness of the insulating CeO_2 layer therefore implies a direct correlation between the J_c of the trilayered sample and the coupling between the top and bottom superconducting layers as the CeO_2 layer thickness is varied.

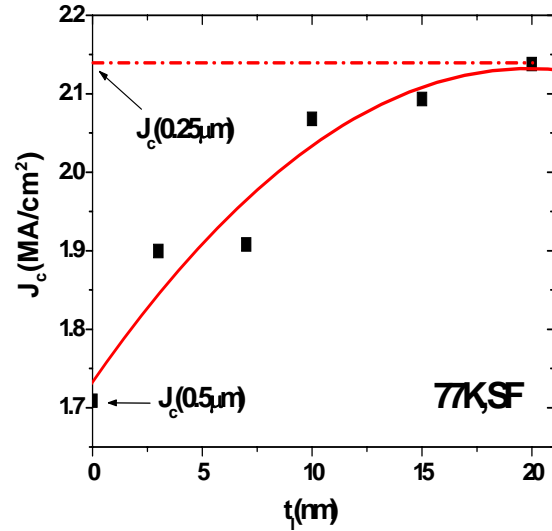


Fig. 4.4: J_c (SF, 77K) of trilayered films as function of CeO_2 thickness t_I (solid square). The solid line represents its polynomial fit. The dash-dot line corresponds to the J_c (SF, 77K) of 0.25 μm thick YBCO film.

4.3 Discussion

A major inconsistency, however, is in the discrepancy between the experimentally measured critical thickness of the insulator $t_I \sim 20$ nm and the theoretically predicted one $6.5\lambda_{ab} \sim 2000$ nm, at which the magnetic interlayer coupling is insignificant. Note that the DC transformer theory is developed on weak pinning system. One hypothesis is that, for strong pinning system YBCO thin film, the decoupling t_I could be much shorter. Unfortunately so far there is no modified theory on strong pinning system available yet but experimentally, it has been demonstrated that for HTS transformer, even at $t_I=50$ nm, the two YBCO layers are still magnetically coupled ^[4.5]. This suggests it is not necessary to completely decouple the YBCO layers in order to realize the sub-layer pinning efficiency. As long as the coupling becomes weak enough and the elastic energy during deformation becomes much less than the pinning energy gained, sub-film (thin film) J_c can be restored in the trilayer.

Note that theoretically in a tri-layer where the two YBCO sub-layers are completely decoupled, the effective L_c becomes equivalent to the thickness of the YBCO sub-layer. Consequently a pseudo thickness-independent J_c is obtained with increasing YBCO layer number as long as the sub-layer thickness is fixed. The tri-layer structure can be generalized into a multi-layer structure and indeed, experimentally a thin film J_c has been realized in a 6-ply multi-layer structure ^[4.6]. Moreover, if one follows the CP theory, the J_c of the multi-layer should be determined by the vortex dynamics of sub-layer. Therefore for a multi-layer structure, although the pinning efficiency is improved

owing to the reduced thickness, the energy barrier against thermal activated flux motion is also reduced. With increasing influence from thermal fluctuation, at certain threshold T or H , the decoupling process will not play any role and CP behavior becomes less important. This has been indeed observed as one compares the J_c – H curves measured at 77K on a single-layer and tri-layer with total YBCO layer thickness of 0.5 μm shown in Figure 4.5. The CeO_2 layer thickness is 20 nm. It can be seen that J_c of the tri-layer drops faster with increasing H than that of single-layer, and at 1 Tesla, J_{cs} of both tri-layer and

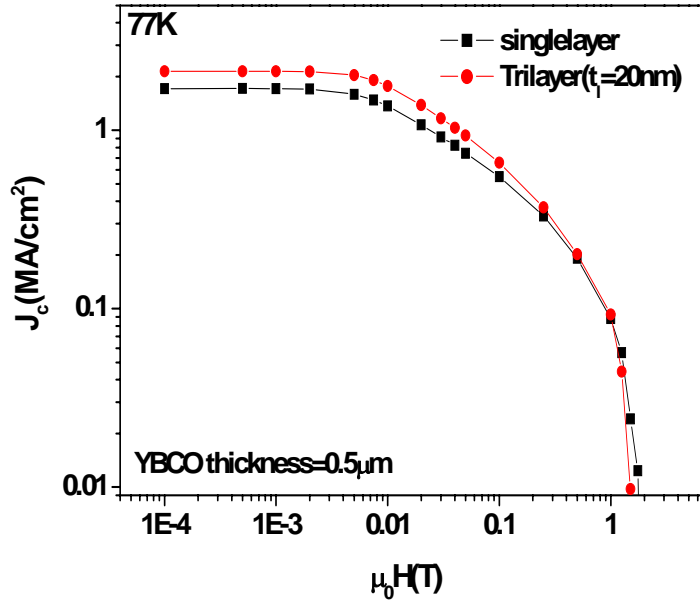


Fig. 4.5: J_c – H curves measured on a single-layer and tri-layer films at 77K. The effective YBCO film thickness is 0.5 μm and the CeO_2 thickness t_l in the tri-layer is 20 nm.

single-layer becomes comparable.

4.4 Summary

In summary, J_c has been studied in $\text{YBa}_2\text{Cu}_3\text{O}_{7-x}/\text{insulator}/\text{YBa}_2\text{Cu}_3\text{O}_{7-x}$ trilayers as the interlayer magnetic coupling is reduced by increasing the thickness (t_I) of the intermediate insulating layer, while the thickness of two $\text{YBa}_2\text{Cu}_3\text{O}_{7-x}$ layer was each fixed at $0.25\text{ }\mu\text{m}$. The experimental results have revealed an intimate correlation between J_c and magnetic coupling and further supported that CP behavior is the underlying mechanism behind the puzzling J_c-t dependence. As expected from the CP theory, the multi-layer approach provides one solution for eliminating J_c-t dependence in YBCO film. However, this approach can only generate a pseudo thickness-independent J_c and within the YBCO sub-layer, J_c-t still maintains. Most importantly, although a thickness-independent F_p can be realized by decoupling vortex into short segments, the F_p is still determined by the random pinning nature within the YBCO sub-layer and is not optimized. With introduction of strong linear defects in as-grown YBCO films, F_p can be optimized and most importantly, made thickness-independent.

CHAPTER 5: J_c - t Elimination Using NTP Insertion

In the previous chapter, we have demonstrated that a pseudo thickness independent J_c could be realized using superconductor/insulator/superconductor tri-layer structure. However, the essence of J_c - t remains untouched and J_c is still determined by the random pinning potential. If one can overpower the random distributed pinning centers by some strong linear defects extending through the film thickness, two positive outcomes are expected: first the F_p is optimized and most importantly, it remains thickness-independent hence leads to a thickness-independent J_c . In this chapter, we will illustrate the method to generate such through-thickness linear defects, so called nanotube pores (NTP) insertion in the YBCO films and reveal the effect of NTP on J_c - t .

5.1 NTP Insertion in YBCO Film

To generate NTPs inside YBCO matrix requires two important components: miscut substrate and nano-particles (NPs) insertion, for controlling mechanical strain on the YBCO lattice at nano-scales. The NPs may be inserted either near the film/substrate interface or during the YBCO film growth. The local tune of the strain by the inserted NPs over the globally strained YBCO lattice on vicinal substrates plays a critical role in pore nucleation, as evidenced from the initiation of pores directly atop the NPs ^[5.1]. A large number of NTPs of dimension from few to hundreds of nanometers form uniformly via self-assembly growth. No degradation occurs to T_c in these samples and the resistivity

in longitudinal direction (along ab-plane) is comparable to that of the typical YBCO films without impurity insertion ^[5.2]. In this section, we report the experimental results on a comparative study of J_c - t behavior between YBCO films with and without inserted NTPs.

Two sets of YBCO films with (YBCO/NTP) and without NTPs (standard YBCO film) were fabricated using PLD technique under similar growth conditions. The YBCO/NTP films were grown on 20° vicinal single crystal (001) SrTiO₃ (STO) substrates while the standard YBCO films, on single crystal (100) LaAlO₃ (LAO) substrates. The laser energy density on the target was ~ 3.2 J/cm² and the repetition rate was 10 Hz. The deposition was carried out onto substrates heated to 765 \sim 775°C in 230 mTorr oxygen partial pressure followed by the annealing in 360 Torr oxygen for 50 minutes. Although the film thickness ranges from 0.09 to 1.2 μ m in this experiment, the samples selected for the J_c - t study have thickness only up to 0.6 μ m to avoid complication of the microstructure degradation in thicker films. After fabrication, silver contact pads were immediately deposited onto the films to minimize the surface resistance. For electrical transport measurement, a 20 \times 400 μ m bridge was patterned using standard photolithography procedure. For YBCO/NTP films, the bridges were parallel to the longitudinal direction, constraining current only in the ab-plane. I-V curves were measured using the standard four-point configuration and a criterion of 1 μ V/cm was applied to determine the J_c .

5.2 Microstructure Analysis of NTP

Figure 5.1 shows the scanning electron microscopy (SEM) images of four YBCO/NTP films with various thicknesses ranging from 0.09 to 0.6 μm . At $t = 0.09 \mu\text{m}$, many pores are already formed in addition to some NPs on the surface. These NPs, which are mostly Y_2O_3 precipitates naturally occurred during the PLD process, serve as the seeds for NTPs to initiate. This means that the densities of NPs and pores are closely

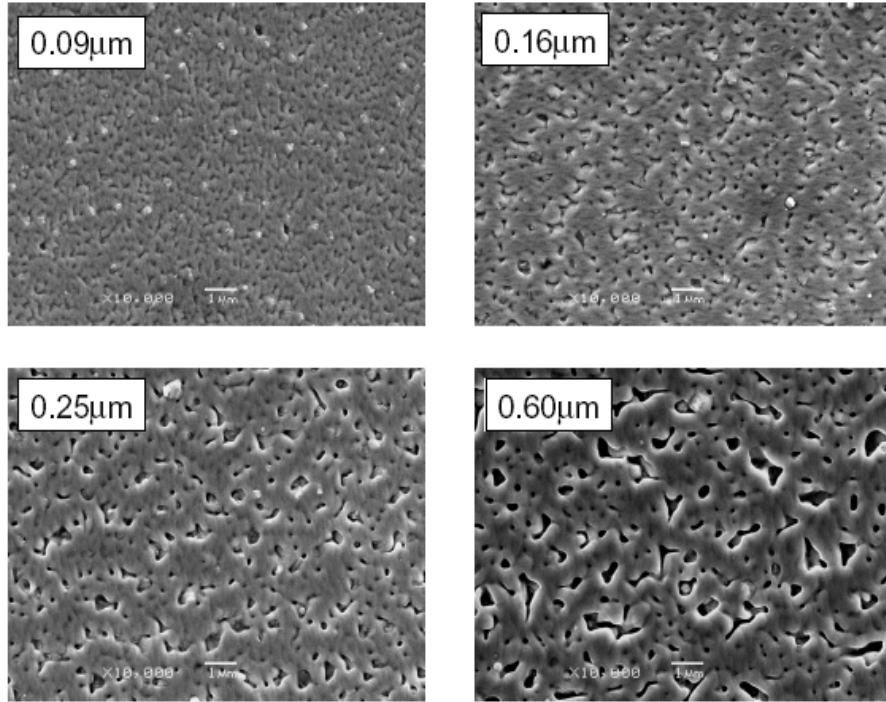


Fig. 5.1: SEM images of YBCO/NTP films at various thicknesses.

correlated ^[5.3]. With increasing t , the density of both NP and pore decrease dramatically and at $t = 0.16 \mu\text{m}$, only few NPs are observed and the pore density n also drops about

50% from $9\text{-}10/\mu\text{m}^2$ to $4\text{-}5/\mu\text{m}^2$. At $t = 0.16 \mu\text{m}$, the visible pores have dimension typically about 100 to 200 nm. It should be mentioned that the pores with smaller dimension are not clearly visible at the magnification used while their presence was confirmed in transmission electron microscopy studies (not shown in this paper). With further increasing thickness, the pore density n remains almost unchanged at around $4\text{-}5/\mu\text{m}^2$ and some large pores of dimension on the order of 500~1000 nm appear as shown on $0.6 \mu\text{m}$ thick sample.

In order to understand how pores evolve through the film thickness, a $1.2 \mu\text{m}$ -thick YBCO/NTP film was thinned via nine consecutive steps using ion milling and

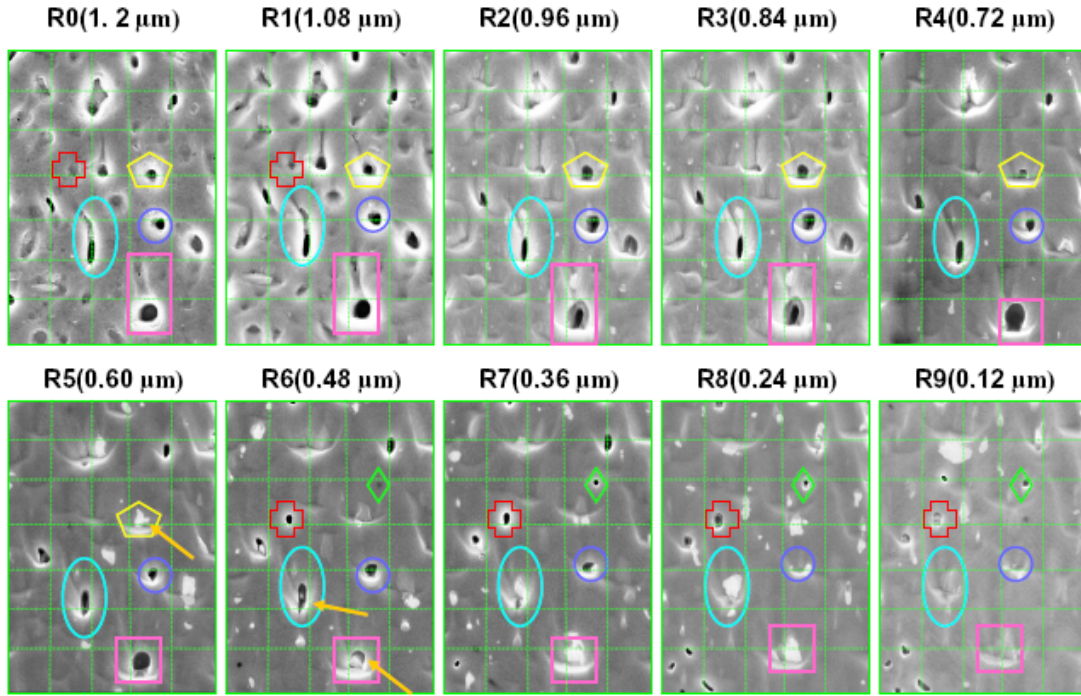


Fig. 5.2: SEM images of a $1.2 \mu\text{m}$ -thick YBCO/NTP film at different stages of thinning using ion milling. R0($1.2\mu\text{m}$) represents the original film and $Rn(d)$ represents the film after n th milling with remaining thickness d . $500\text{nm}\times 500\text{nm}$ grids are applied to each image and a colored pattern is used for tracking a specific NTP through different layers of thickness.

analyzed using SEM after each step of 0.12 μm thinning. Marks were employed so that the same pores can be monitored through the milling steps. Figure 5.2 includes the SEM images taken on the original sample surface (R0) and on each of the nine steps of milling (R1 through R9). Many pores can be traced through different layers of the film and most of them are almost through the entire (for example, the three pores labeled respectively with cyan ovals, blue circles, and pink squares)

or a large portion (green diamonds for a pore through the bottom half of the film and yellow pentagons for a pore through the top half) of the film thickness. This means that they have NT geometry. We have also observed some pores closed at certain thickness and reappear (red crosses). Y_2O_3 NPs, which were confirmed with energy-dispersive x-ray spectroscopy, are visible at the bottom of NTPs (a few marked

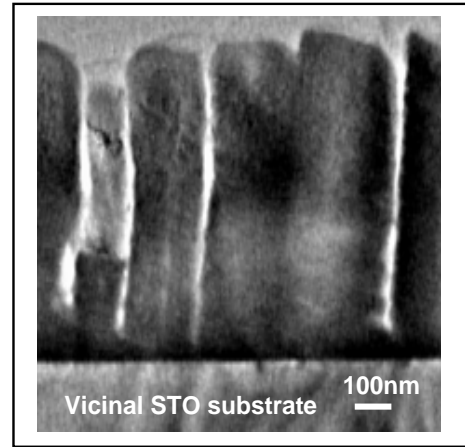


Fig. 5.3: Cross-sectional TEM of a 1.0 μm -thick NPT/YBCO film.

with yellow arrows), confirming that NPs indeed play a critical role in nucleation of the NTPs. It should be noted that the density of the Y_2O_3 NPs is at least an order of magnitude smaller than that near the film/substrate interface ^[5.3]. Above $t=100$ nm, the NP density is on the order of $0.2\text{-}0.3/\mu\text{m}^2$. In the thickness range from 0.16 μm to 0.6 μm , the density of the pore in YBCO/NTP films is more or less a constant, which agrees with Figure 5.1. This suggests that number of newly-generated NTPs is comparable to that of disappeared NTPs in this thickness range, while the majority NTPs initiate at smaller thickness. Interestingly, most NTPs appear at the same or close to the same lateral

location at different thickness while their lateral dimension experiences some increases through the 1.2 μm film thickness. This means that they are more or less straight nanotubes aligned along the normal of the film. In order to further confirm that NTPs are through most of the film thickness, a cross-sectional transmission electronic microscopy (TEM) picture was taken on a 1.0 μm -thick NTP/YBCO film and shown in Fig. 5.3. It can be seen clearly that NTP, indicated by the white lines, are indeed through most of the film thickness.

5.3 J_c of YBCO Film Before and After NTP Insertion

In Fig. 5.4, the J_c at SF and 77 K is plotted as function of thickness for both YBCO/NTP (squares) and standard YBCO (circles) samples. Considering the possible nonuniformity of NTPs in the YBCO/NTP sample at smaller thickness, only the J_c of the films with thickness in the range of 0.16 to 0.6 μm -thick film are included. The solid lines are guides for eyes.

There are two interesting observations in Fig. 5.4. First, the J_c values of the YBCO/NTP films are overall higher than that of the standard YBCO films in the same

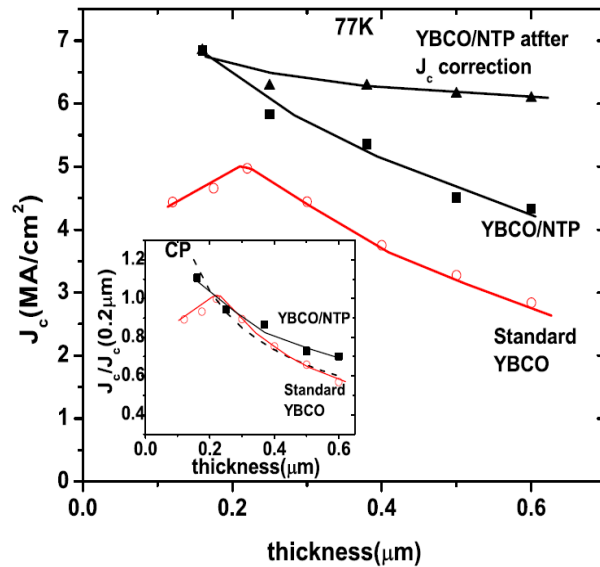


Fig. 5.4: J_c-t curves of YBCO standard films (circles) and YBCO/NTP films (squares) at 77 K and SF. Also shown is the J_c-t curve of YBCO/NTP (triangles) assuming a thickness-independent NTP lateral dimension. Inset shows the J_c-t curves of the two types of films in a normalized scale $J/J_c(0.2\mu\text{m})$. The same symbols as in Fig. 5.4 are employed for the two curves in the inset. The dash line indicates the fitting of the CP model.

thickness range. At $t=0.25\text{ }\mu\text{m}$, the J_c of the YBCO/NTP sample is 5.83 MA/cm^2 , which is $\sim 20.7\%$ higher than that of the standard YBCO sample and at $t=0.6\text{ }\mu\text{m}$, it is $\sim 52.8\%$. Note that the J_c values of the standard YBCO samples are between 5.0 to 2.8 MA/cm^2 at $0.2\text{ }\mu\text{m} \leq t \leq 0.6\text{ }\mu\text{m}$, which are comparable to the typical J_c s around 5.5 to 3.5 MA/cm^2 reported in the same thickness range ^[5.4, 5.5]. On the other hand, the YBCO/NTP films experience weaker thickness dependence of J_c than the standard ones do. This latter observation can be further illustrated in the inset of Fig. 5.4 by replotting the two curves in Fig. 5.4 on a normalized scale $J_c/J_c(0.2\text{ }\mu\text{m})$. With increasing t from 0.25 to $0.6\text{ }\mu\text{m}$, for example, J_c drops only 26% for the YBCO/NTP films as opposed to a 40% reduction on the standard YBCO films. Moreover, the J_c-t of the standard YBCO films can be well fitted by $J_c \propto t^{1/2}$ as predicted by modified CP model in most of the thickness range except the deviation below $0.2\text{ }\mu\text{m}$. This deviation, which leads to a switch from increasing J_c to decreasing J_c with increasing t , has been observed previously ^[5.6-5.8]. In Chapter 3, we argued that this deviation from $J_c \propto t^{1/2}$ is most probably related to the pronounced TAFM since a shorter vortex collectively pinned by point defects is more easily thermally activated than a longer one within L_c . In contrast to the standard films, such switch is not observed in the according thickness range for YBCO/NTP, suggesting that the TAFM is greatly suppressed as point defect pinning is overpowered by NTP pinning.

Although a weaker thickness dependence of J_c is observed in the YBCO/NTP samples, the remaining J_c-t is unexpected if NTP dominates the pinning. A possible explanation is the reduced cross-sectional area owing to those enlarged NTPs at larger thickness, which leads to an underestimated J_c in thick films. To quantify this argument,

the NTPs' lateral dimension increase, which translates to reduction of the cross-sectional area for the electrical current, was estimated based on the SEM images shown in Fig. 5.1. When t increases from 0.16 μm to 0.25 μm , the reduced current cross-sectional area is about 7%. It increases to $\sim 29\%$ when t is increased to 0.6 μm . Considering the correction of the cross-sectional area, an “ideal” J_c - t curve is extracted and added in Fig. 5.4 (triangles). It is not surprising that the J_c - t curve of YBCO/NTP films with perfectly straight NTPs drops only $\sim 5\%$ as thickness increases from $\sim 0.25 \mu\text{m}$ to 0.6 μm . This greatly weakened J_c - t clearly demonstrates that NTP insertion is indeed an effective approach to eliminate J_c - t by providing a thickness independent F_p . In addition, the ideal NTP's lateral dimension should be on the order of the coherence length in ab-plane ξ_{ab} ($\sim 3.5 \text{ nm}$ for YBCO at 77 K) ^[5.9, 5.10]. Higher J_c values are anticipated in YBCO/NTP films if the lateral dimension of the NTP could be reduced to a few nanometers close to ξ_{ab} .

Based on the observed NTP's density in Fig. 5.1, the matching field $H_m = n\Phi_0$ is estimated to be about 8~10 mT. The actual H_m may be slightly higher due to those uncounted smaller NTPs in few to tens of nanometer regime. As the applied magnetic field H exceeds H_m , some vortices will no longer be pinned by the NTPs. Instead, they will be pinned by other weaker pinning centers. With increasing H , the NTP will gradually render the dominancy to those weaker pinning centers. These weaker pinning centers are most likely isotropic ones such as secondary phase inclusions. Consequently, the CP-type J_c - t curves observed in the standard YBCO samples will be resumed in YBCO/NTP samples at a certain $H \gg H_m$. This argument seems to agree well with the

enhanced thickness dependence of J_c in the YBCO/NTP samples at $H > H_m$ as shown in Fig. 5.5(a). Note that the J_c of the YBCO/NTP samples in Fig. 5.5(a) and hereafter are

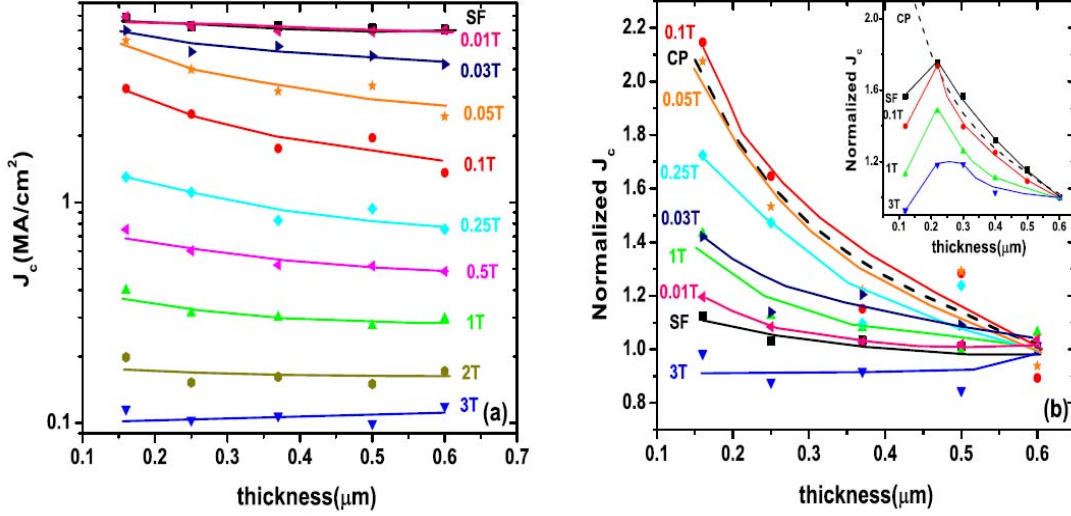


Fig.5.5: (a) J_c - t curves of YBCO/NTP films at 77 K and various H fields. Solid lines are drawn to guide eyes; (b) J_c - t of YBCO/NTP and standard YBCO films (inset) at 77 K and various H in a normalized scale $J_c/J_c(0.6\mu\text{m})$. The dash line indicates the fitting of the CP model.

calculated using the effective cross-sectional area and H is applied along film normal. The effect of H on the J_c - t behavior of the YBCO/NTP films is further quantified in Fig. 5.5(b) in which most of the curves in Fig. 5.5(a) are replotted on a normalized scale [$J_c/J_c(0.6\mu\text{m})$]. For comparison, the inset of the Fig. 5.5(b) shows the normalized J_c - t curves measured on the standard YBCO films. It can be seen that the J_c - t curve of the YBCO/NTP films gradually evolves into CP-type with increasing H . At around 0.05 to 0.1 Tesla, it shows a close resemblance to $J_c \propto t^{-1/2}$ indicated by the dashed line, suggesting the dominance of the collective pinning by point defects as H is around $10H_m$. Note that this H range (0.05 to 0.1 Tesla) is exactly where the two types of film show comparable J_c , also suggesting a similar pinning mechanism in this field range. With

further increasing H , the effect of the TAFM becomes visible and more enhanced at higher H , which continuously weakens the J_c-t of the YBCO/NTP samples in a similar way as in the case of the standard YBCO samples shown in the inset. This complex effect of H on J_c-t indicates the existence of dual pinning systems in the YBCO/NTP films and suggests that higher density straight NTPs are necessary to extend a flat J_c-t to higher H fields.

5.4 Conclusions

In summary, we have fabricated YBCO/NTPs films and studied their J_c-t behavior at 77 K and various magnetic fields up to 5T. Since the NTPs are linear defects aligned along the normal of the film and through nearly entire film thickness, they provide an enhanced pinning force F_p on each vortex, which remains independent of film thickness. The enhanced pinning by NTPs results in high J_c values and effectively suppresses the TAFM. In addition, the t -dependence of J_c observed in the standard YBCO films is much reduced in the YBCO/NTP samples at $H < H_m$ and may be completely eliminated when the NTPs' lateral dimension is made constant. Interestingly, the CP-type J_c-t behavior is resumed in YBCO/NTP samples at $H \gg H_m$, which suggests a switch from the stronger NTP pinning to the weaker point defect pinning.

Although J_c shows weak thickness dependence after NTP insertion, macroscopic J_c still shows thickness dependence owing to NTP evolution with increasing thickness. Therefor it brings complication to precisely quantifying the effect of linear defects on J_c-t . It then necessitates the further J_c-t investigation in a system with consistent pinning landscape at any given thickness.

CHAPTER 6: J_c - t Elimination Using BZO NRD Insertion

In previous chapter, we have demonstrated that thickness dependence of J_c could be effectively weakened with NTP insertion. Since majority of NTP are through the entire film thickness, they provide an optimized F_p which remains constant with changing thickness. However, complication is generated since NTP's diameter increases with thickness. In order to obtain a uniform pinning structure less affected by thickness, we will turn to the other widely used method to generate linear defects in YBCO films: impurity insertion.

Among all the reported methods of impurity insertion in YBCO films, BaZrO_3 (BZO) nano-particles (NP) insertion remains to be the most interesting one since the BZO NPs are capable of self-aligning themselves into columnar shape^[6.1]. However, it is also known that the defect landscape of BZO doped YBCO films (YBCO/BZO) can be very different for various BZO concentrations and fabrication methods. This of course, would strongly influence superconducting properties for YBCO/BZO samples fabricated using different methods. A systematic study on PLD YBCO/BZO films suggests that both T_c and SF J_c linearly decreases with BZO volume fraction^[6.2]. A significant 2 to 3 K T_c and + 50% SF J_c degradation was reported in the PLDed YBCO films after only 2% BZO NP insertion. However no such degradation was observed in the TFA-MOD YBCO film even after 10% BZO NP insertion^[6.3]. Microstructure study on these films revealed that, for the latter case, BZO NPs randomly distributed in the YBCO matrix instead of forming aligned nanorods (NRDs) as in the PLD films. In addition to that, the profile of

the angular dependence of J_c also indicated that, while the better ab-plane integrity was observed in the latter case, the so-called “buckling effect” of ab-plane was much more pronounced in the PLD YBCO/BZO films with self-assembled BZO NRDs^[6,4].

The mechanism of BZO NRDs self-assembly is of great importance for the application of 2G HTS wire since it holds the key to the optimized pinning structure and elimination of J_c-t in HTS films. Computer simulation suggests that the tremendous strain field caused by the +8.7% lattice mismatch between BZO and YBCO is critical for the vertical alignment during the *in-situ* heteroepitaxial growth. Specifically this stress-mediated ordering results in a simultaneous phase separation and grouping during the layer-by-layer growth^[6,4]. In other words, the BZO NPs tend to align itself in the growth front to maintain the lowest energy scheme. Therefore it is expected that growth temperature may have a significant effect on the BZO NPs self-assembly since it dictates the mobility of BZO NP. This immediately renders the possibility that the thickness dependence of J_c could be very different for PLD YBCO/BZO films fabricated at different temperatures due to the possible difference in the pinning landscape. In this chapter, we report the growth temperature effect on J_c of the YBCO/BZO films followed by the thickness dependence of J_c in these films.

6.1 Growth Temperature Effect on J_c of YBCO/BZO

Two groups of YBCO/BZO films were fabricated using PLD technique at 790 and 810°C on single crystal (100) LaAlO₃ (LAO) substrates. In the rest of this chapter, group A refers samples grown at 790 °C and group B, at 810 °C respectively. This sets the only difference between these two groups of samples in terms of growth conditions. The BZO volume fraction is 2% for both groups of films. The laser energy density on the target was $\sim 3.2 \text{ J/cm}^2$ and the repetition rate was 8 Hz. The deposition was carried out in 300 mTorr oxygen partial pressure followed by the annealing in 760 Torr oxygen at 500°C. The samples selected for the J_c - t study have thicknesses only up to 0.6 μm to avoid complication of the microstructure degradation in thicker films. Most of the superconducting properties of the sample were characterized using a Quantum Design SQUID magnetometer. For electrical transport measurement such as angular dependence of J_c , a 20×400 μm bridge was patterned using photolithography. The I - V curve was measured with the standard four-point configuration and the criterion of 1 $\mu\text{V/cm}$ was applied to determine the J_c . The stage where samples were mounted can be rotated with respect to the applied magnetic field H . The direction of J was always maintained perpendicular to the H to enable the maximum Lorentz force scheme. The major microstructural information was retrieved using cross-sectional transmission electron microscopy (TEM).

Fig. 6.1 shows the comparison of J_c between the two groups of films as function of applied magnetic field in a semi-log scale at 77 K. Each group includes two films with thickness of 0.2 and 0.6 μm . Open symbols correspond to J_c measured on group A and solid ones, on group B. It can be seen that, at field regime lower than 1500 Oe, J_c s are

comparable for both groups of samples regardless of film thickness. Specifically, SF J_c is around $1.35\text{MA}/\text{cm}^2$ for group A and $1.45\text{MA}/\text{cm}^2$ for group B. With further increasing field, J_c of group A drops much faster than that of group B. For example, at 1 Tesla, J_c of the $0.6\mu\text{m}$ -thick film from

group B is about $0.08\text{MA}/\text{cm}^2$, which is already twice of that from group A. This J_c difference keeps increasing with field, suggesting a significantly enhanced flux pinning in samples from group B. The

comparison of J_c - H curves between two groups provides

evidence supporting the argument that higher growth temperature might increase the chance of the BZO NP self-assembly. To further test the existence of correlated pinning, we also measured angular dependence of J_c on the $0.2\mu\text{m}$ -thick films from the two groups and the result is plotted in Fig. 6.2 with that of $0.18\mu\text{m}$ -thick PLD YBCO film without BZO NP addition (referred as the standard film hereafter). The measurement was conducted at 77 K and 1 Tesla and θ represents the angle enclosed between applied magnetic field and film normal (c-axis). One can immediately notice that the group B sample has the signature of strong correlated pinning along the c-axis — a J_c peak as

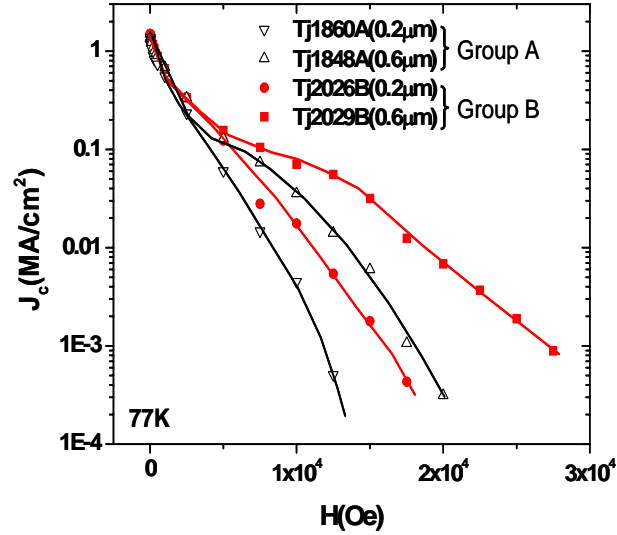


Fig.6.1: J_c as function of applied magnetic field H for two groups of YBCO/BZO grown at 790 and 810°C at 77 K.

$H//c$ -axis. Due to the absence of this c -axis J_c peak, the presence of BZO NRDs in the group A remains a question.

However, intuitively one may wonder that the 20°C difference in the growth temperature may not be enough to completely randomize the distribution of the BZO NPs.

Another possible reason responsible for the absence of this J_c peak could be the low density of BZO NRDs. This seems to be a reasonable argument at least based on the difference of J_c peak between the two groups of samples as H is parallel to the ab -plane. Owing to the large stress field generated by the +8.7% lattice mismatch between BZO and YBCO, the damage of integrity and continuity of ab -plane is inevitable

and therefore the intrinsic pinning as well as the J_c is suppressed when $H//ab$ -plane. Hence it is not hard to imagine that the “buckling effect” increases, or $J_c(H//ab\text{-plane})$ decreases with the increasing density of BZO NRDs. For the standard sample, since dominant defects are randomly distributed point pins (similar to the TFA-MOD YBCO/BZO film), the ab -plane integrity is well maintained and an pronounced $J_c(H//ab\text{-plane})$ peak is observed. This probably explains why J_c of group A falls just in between that of the standard sample and group B when $H//ab$ -plane.

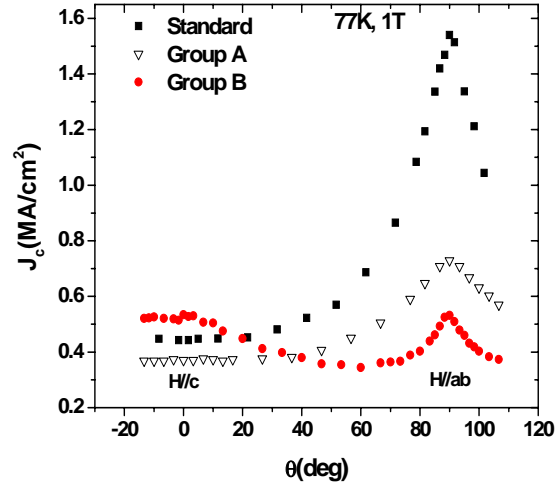


Fig. 6.2: J_c as function of θ , which is the angle enclosed between applied magnetic field and film normal for two representative 0.2 μm -thick YBCO/BZO films from group A and B. A similar curved measured on a 0.18 μm -thick standard YBCO film is also plotted together.

Based on the above observation and analysis, the effect of growth temperature on the pinning landscape of PLD YBCO/BZO samples can be summarized as the following: higher growth temperature increases the chance of the BZO NRDs self-assembly. This leads to a higher density of such through-thickness linear defects in group B than that of group A. The pinning landscape of group A is most likely consists of two types of defect: a few through-thickness BZO NRDs and large number of short BZO NRD segments. The density of former can be simply estimated using $n=B^*/\Phi_0$, where B^* is about 1500 Gauss and $\Phi_0=2.07\times 10^{-7}\text{G}\cdot\text{cm}^2$ is the flux quanta. This gives n about $75/\mu\text{m}^2$.

6.2 Growth Temperature Effect on Pinning Structure

Fig. 6.3 shows the cross-sectional transmission electron microscopy (TEM) images of two representative samples from group A and group B. Unfortunately the TEM of group A is not very clear so it seems impossible to accurately quantify the NRD's density at this moment. However several through-thickness BZO NRDs are still

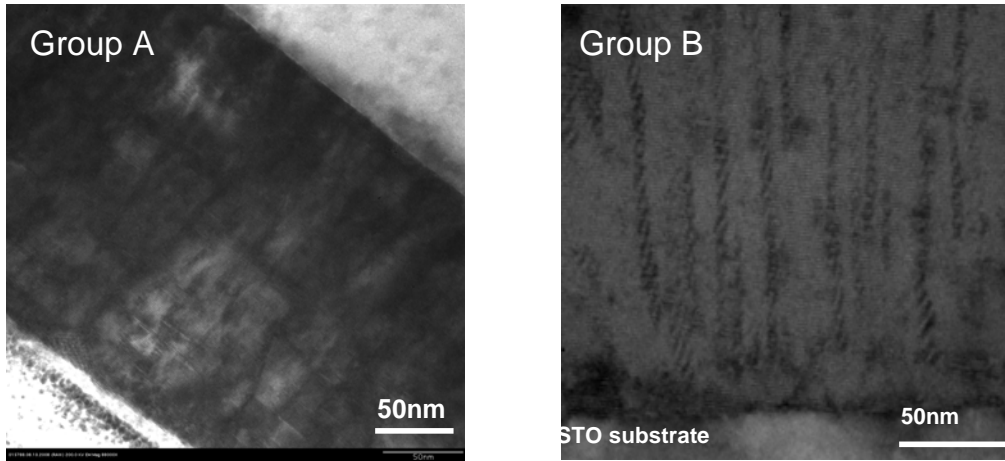


Fig. 6.3: Cross-sectional TEM images from two representative samples from group A and B. Unfortunately the TEM of group A is not very clear but several through-thickness NRD are still visible. On the other hand, the TEM image of group B sample shows dense and well aligned BZO NRDs.

visible, which confirms the existence of correlated pinning in the group A sample. On the other hand, the TEM image of the group B sample shows well aligned BZO NRDs with density around $1600/\mu\text{m}^2$, giving a match field around 3.2 Tesla.

6.3 Elimination of J_c - t in Low H Regime

Since samples from both groups share the same pinning mechanism — the strong correlated pinning along c-axis in the low field regime less than 1500 Gauss, a thickness independent J_c should be observed as already implicitly shown in Fig. 6.1 for $t = 0.2$ and $0.6 \mu\text{m}$. To further illustrate this point,

J_c s of samples from both group A are plotted as function of thickness at 77 K and various fields in Fig. 6.4. The solid lines and dashed lines are guides for eyes of data points measured on group A and group B, respectively. It can be seen that both groups have thickness-independent J_c in the low field regime when $B < 0.1$ Tesla. As B further increases, group A samples start to develop thickness

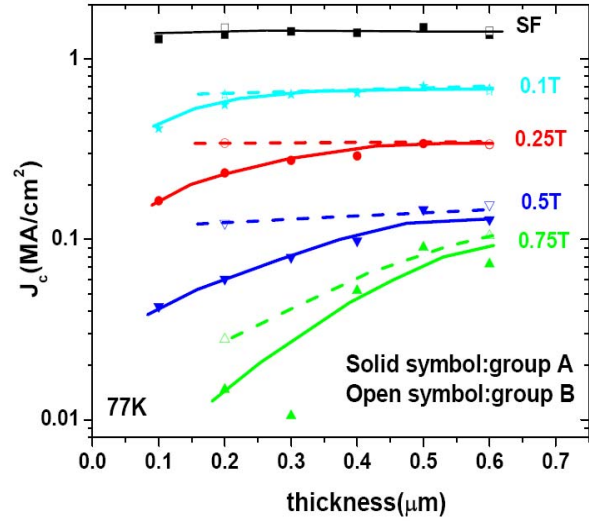


Fig. 6.4: J_c as function of thickness measured on group A and B at 77 K and various magnetic fields. Solid lines and dashed lines are guides for eyes of data points from group A and group B respectively.

dependence while for group B sample, the thickness-independent J_c has been well maintained even up to 0.5 Tesla. Note that the BZO NRD's density of group B samples is much higher than that of group A, it is not surprising that J_c could be maintained almost

thickness-independent in a larger field range for sample grown at high temperature. On the other hand, since thinner films are always more vulnerable to the pronounced TAFM disregarding the pinning mechanism, it inevitably would result in a reversed J_c-t as indicated by the both curves at 0.75 Tesla.

6.4 Lower SF J_c Observed After BZO Insertion

Note that J_c-t elimination using BZO NRD insertion again supports the conclusion that the collective pinning mechanism has the strong correlation with the observed J_c-t in standard YBCO films. This observation is consistent with our previous results on YBCO/NTP samples shown in chapter 5. However a distinct difference

between YBCO/BZO and YBCO/NTP is the SF J_c value.

Even comparing with standard films at 77 K, J_{cs} of YBCO/BZO films drop typically 30% to 60%(depends on film thickness) than that of standard samples. Interestingly, the J_c difference also depends

on temperature, as shown in Fig. 6.5, in which $J_c(SF)$ as function of temperature of these

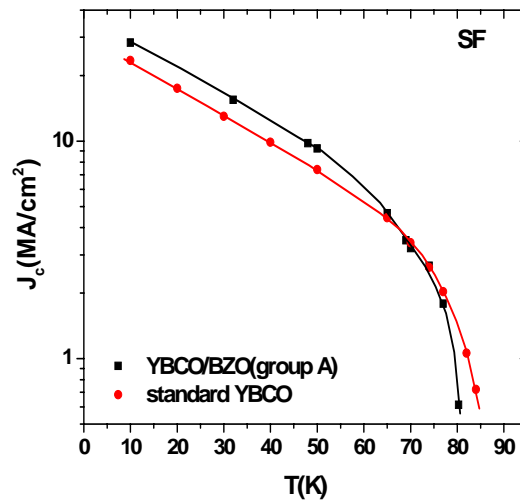


Fig. 6.5: J_c-T measured on two 0.6 μ m-thick films with and without BZO NRD insertion. A J_c crossover is observed at 70 K. A semi-log plot is applied to show the scaling behavior below 50 K.

two types of films with thickness of 0.6 μm are plotted together. It can be seen that the J_c difference is rapidly vanishing with decreasing T and even reversed at T below 50 K. An important observation here is that J_c of these two types of films can numerically scale to each other at the same thickness below 50 K. The scaling factor $J_c(\text{YBCO/BZO})/J_c(\text{YBCO})$ is about 1.25. Since the pinning structure is not likely altered by varying temperature for both types of film, this scaling correlation probably implies a difference in the superconductor volume. Considering large stress field as well as slight poisoning in the YBCO matrix around BZO NRDs, a shell of highly disordered YBCO layer could be formed with T_c gradually degraded from 90 K to 50 K while approaching the BZO NRD. Since the T_c of YBCO/BZO sample is only around 86 to 87 K, the disturbed YBCO crystalline could be global for both group A and B regardless the growth temperature. In addition to the suppressed T_c , J_c is also greatly reduced due to the limited superconductor volume, which shrinks further with increasing temperature above 50 K. At T below 50 K, the superconductor volume becomes T independent but could be still smaller than that of standard YBCO film. This probably explains that YBCO/BZO film's J_c is much lower than that of YBCO/NTP film even though they share a similar pinning mechanism. Another important feature in this low T region is that the J_c of both types of films exponentially increases with decreasing T . This similar J_c - T dependence, as predicted by flux creep model, seems to be independent of pinning mechanism^[6,3].

Although the addition of BZO NPs can effectively eliminate the J_c - t by self-assembling them into through-thickness linear defects, the large lattice strain also generates unavoidable side effect — reducing the superconductor volume considerably. It is worthy noticing that several attempts have been made to minimize this collateral

damage. One of them is to apply material with less lattice mismatch than that of BZO/YBCO. Several works on BSnO_3 addition in YBCO have been published and the results indicate that at least T_c of ~ 90 K was recovered as the lattice mismatch is reduced from 8.7% to 7.7% ^[6.5, 6.6]. Similar results have been also obtained when YBCO/BZO film is grown on a small miscut angle ($\sim 5^\circ$) vicinal substrate ^[6.7]. It is also possible to modify the post-annealing condition to minimize the lattice relaxation across the interface between BZO and YBCO. Therefore the degraded YBCO matrix could be confined in the vicinity of the BZO NRD. Practically this approach has been studied using the quench annealing we developed earlier ^[6.8]. Our preliminary results indicated that T_c was improved by 3 K to around 89 K and SF J_c by 28% as compares YBCO/BZO samples with different annealing conditions.

6.5 Conclusions

In summary, we have fabricated YBCO/BZO films at different temperatures and investigated its effect on the sample's defect structure. Both superconductivity and microstructure analysis suggest that higher growth temperature benefits the self-assembly of BZO NRDs, which results in a higher density of through-thickness NRDs in group B samples. Despite the difference in the NRD's density, the correlated pinning along the c-axis provides a constant pinning force F_p at variable thickness, hence results in a thickness-independent J_c at low field regime for YBCO/BZO samples from both groups. The contradiction between the enhanced pinning by BZO NRDs and relatively lower SF J_c could be explained by the large stress field around the BZO NRD, which leads to a considerably reduced superconductor volume. While this stress field is essential for the

BZO self-assembly, developing strategies to control the damage is crucial for further improving the performance of the 2G YBCO coated conductor.

CHAPTER 7: CONCLUSIONS

Since the discovery of HTS materials in 1986, the promise of zero-dissipation devices operating at liquid nitrogen boiling temperature has fuelled a world wide research investment worth billions of US dollars. The major obstacle preventing its wider commercialization is the high production cost owing to its ceramic nature. Even though it is generally true that HTS coated conductor's extraordinary current carrying capability translates to lower cost, further improving its performance/cost ratio is still the focus among the HTS community. However, the long standing issue of thickness dependence of critical current density greatly jeopardizes these efforts. In order to shed light on the underlying mechanism of this mysterious J_c-t , we systematically studied the temperature and magnetic field effect on J_c-t . The remarkable consistency between the experimental results and the CP theory suggests that J_c-t is most likely the result of the collective pinning behavior of a random pinning potential, and thermal fluctuations systematically change it in a predictable way. Therefore, the key to J_c-t elimination is to maintain a thickness-independent pinning force line density, F_p , which can be realized by either changing the vortex structure or the pinning structure.

We tested the first approach by constructing a HTS/Insulator/HTS trilayer structure. Indeed we observed the J_c of the trilayer monotonically increases with the insulator thickness t_I , and at $t_I \sim 20$ nm, the sub-layer J_c is restored in the trilayer structure. However, this trilayer approach only gives a pseudo thickness-independent J_c , and most importantly, its J_c is dominated by the random pinning potential which is not optimized.

The most effective approach to eliminate J_c-t would be directly overpowering the point pins with strong linear defects. This approach has been realized with either NTP or BZO NRD insertion. For the former case, J_c-t is still present even though it becomes weaker. We attribute this weaker J_c-t to a smaller cross-sectional area in a thicker film due to the NTP enlargement with increasing film thickness. Owing to NTP's small density, the thickness-independent J_c is only maintained in a very low field regime and by further increasing the applied magnetic field, the CP-like J_c-t is restored. The latter case of BZO NRD insertion provides a uniform pinning landscape across the entire thickness range of interest. Consequently, the as-measured J_c shows nearly no thickness dependence. Unfortunately, it is still not a perfect approach since the BZO nano-particles significantly distort the surrounding YBCO matrix, leading to the considerably reduced J_c at self-field.

Further improvement of the linear defect insertion relies on a better control of the defect's dimension, density and interface. Endeavors are being devoted to a thorough understanding of the nucleation and growth mechanisms of these linear defects in our group.

REFERENCES:

CHAPTER 1

- [1.1] H. Kamerlingh Onnes, Leiden Comm. **120b, 122b, 124c**(1911).
- [1.2] W. Meissner and R. Ochsenfeld, Naturwissenschaften **21**, 787(1933).
- [1.3] J. Bardeen, L. N. Cooper and J. R. Schrieffer, Phys. Rev. **108**, 1175(1957).
- [1.4] G. Bednorz and K. A. Müller, Z. Phys. **B64**, 189(1986).
- [1.5] F. and H. London, Proc. Roy. Soc. (London) **A149**, 71(1935).
- [1.6] A. B. Pippard, Proc. Roy. Soc. (London) **A216**, 547(1953).
- [1.7] V. L. Ginzburg and L. D. Landau, Zh. Eksperim. i Teor. Fiz. **20**, 1064(1950).
- [1.8] A. A. Abrikosov, Zh. Eksperim. i Teor. Fiz. **32**, 1442(1957).
- [1.9] J. Bardeen and M. J. Stephen, Phys. Rev. **140**, A1197(1965).
- [1.10] M. K. Wu *et al.*, Phys. Rev. Lett. **58**, 908(1987); Z. X. Zhao *et al.*, Kexue Tongbao **33**, 661(1987).

CHAPTER 2

- [2.1] K. Heine, J. Tenbrink and M. Thoner, Appl. Phys. Lett. **55**, 2441(1989).
- [2.2] Y. Iijima, N. Tanabe, O. Kohno and Y. Ikeno, Appl. Phys. Lett. **60**, 769(1992).
- [2.3] V. Selvamanicam *et al.*, Phys. C doi: 10.1016/j.physc.2007.04.236(2007).
- [2.4] M. Rupich *et al.*, presentated in US Department of Energy Wire Development and Application Workshop 2007; available at www.energetics.com/wire07/agenda.html.
- [2.5] A. Ibi *et al.*, Physica C **445-448**, 525(2006).
- [2.6] R. A. D’Errico, SuperPower announces first major wire shipment. The Business Review (December 20, 2006).
- [2.7] M. Tachiki and S. Takahashi, Solid State Communications **72**, 1083(1989).

- [2.8] B. Roas, L. Schultz and G. Saemann-Ischenko, Phys. Rev. Lett **64**, 479(1990).
- [2.9] M. Hawley, I. D. Raistrick, J. C. Beery et al, Science **251**, 1587(1991).
- [2.10] Ch. Gerber, D. Anselmetti, J.G. Bednorz et al, Nature **350**, 280(1991).
- [2.11] B. Dam, J. M. Huijbregtse, F. C. Klaassen et al, Nature **399**, 439(1999).
- [2.12] R. Griessen, Wen Hai-hu, A. J. J. Van Dalen et al, Phys. Rev. Lett. **72**, 1910(1994).
- [2.13] C. J. Can der Beek and M. Konczykowski, Phys, Rev. B. **66**, 024523(2002).
- [2.14] A. Catana, R. F. Broom, J. G. Bednorz, Appl. Phys. Lett. **60**, 1016(1992).
- [2.15] T. I. Selinder, U. Helmersson, Z. Han et al, Physica C **202**, 69(1992).
- [2.16] K. Verbist, A. Kule and A. Vassiliev, Physica C **269**, 131(1996).
- [2.17] D. Larbalestier *et al*, 2006 DOE Peer Review.
- [2.18] R. L. S. Emergo, J. Z. Wu *et al*, Appl. Phys. Lett. **87**, 232503 (2005).
- [2.19] P. W. Anderson, Phys, Rev. Lett. **9**, 309(1962).
- [2.20] Y. Yeshurun and A. P. Malozemoff, Phys, Rev. Lett. **60**, 2202(1988).
- [2.21] Y. B. Kim, C. F. Hempstead and A.R. Strnad, Phys, Rev. Lett. **9**, 306(1962).
- [2.22] I. A. Campbell, L. Fruchter and R. Cabanel, Phys, Rev. Lett. **64**, 1561(1990).
- [2.23] H. M. Smith and A. F. Turner, Appl. Opt. **4**, 147(1965).
- [2.24] D. Dijkkamp, T. Venkatesan and X. D. Wu *et al.*, Appl. Phys. Lett. **51**, 619 (1987).
- [2.25] T. Aytug, M. Paranthaman and A.A.Gapud *et al.*, J. Appl. Phys. **98**, 114309(2005).
- [2.26] P. Mele, K. Matsumoto and T. Horide *et al.*, Physica C **445-448**, 648(2006).
- [2.27] T. Haugan, P. N. Barnes, and R. Wheeler *et al.*, Nature **430**, 867(2004).
- [2.28] Y. Yamada, K. Takahashi, H. Kobayashi *et al.*, Appl. Phys. Lett. **87**, 132502(2005).
- [2.29] J. G. Lin and C. Y. Huang *et al.*, Phys. Rev. B **51**, 12900(1995).

- [2.30] A. K. Pradhan, M. Murakami and N. Koshizuki, Supercond. Sci. Technol. **13**, 761(2000).
- [2.31] C. P. Bean, Rev. Mod. Phys. **36**, 31 (1964).
- [2.32] E. M. Gyorgy, R. B. Vandover and K. A. Jackson *et al.*, Appl. Phys. Lett. **55**, 283(1989).
- [2.33] A. Gurevich and E. H. Brandt, Phys, Rev. Lett. **73**, 178(1994).
- [2.34] J. R. Thompson, Ö. Polat and D. K. Christen *et al.*, Appl. Phys. Lett. **93**, 042506(2008).
- [2.35] G. Blatter, M. V. Feigel'man, V. B. Geshkenbein, A. I. Larkin and V. M. Vinokur, Rev. Mod. Phys. **66**, 1125(1994).
- [2.36] D. K. Christen and J. R. Thompson, Nature **364**, 96(1993).
- [2.37] S. R. Foltyn, P. Tiwari, R. C. Dye *et al*, Appl. Phys. Lett. **63**, 1848(1993).
- [2.38] S. R. Foltyn, Q.X. Jia, P. N. Arendt *et al*, Appl. Phys. Lett. **75**, 3692(1999).
- [2.39] B. W. Kang, A. Goyal, D. F. Lee *et al*, J. Mater. Res., **17**, 1750(2002).
- [2.40] Q. X. Jia, H. Wang and Y. Lin *et al*, IEEE Tran. Appl. Supercond. **17**, 3234(2007).
- [2.41] Q. X. Jia, S. R. Foltyn, P. N. Arendt *et al*, Appl. Phys. Lett. **80**, 1601(2002).
- [2.42] S. R. Foltyn, H. Wang, L. Civale *et al*, Appl. Phys. Lett. **87**, 162505(2005).
- [2.43] S. Miura, K. Hashimoto, F. Wang *et al*, Physica C **278**, 201(1997).
- [2.44] A. Ignatiev, Q. Zhong, P.C. Chou *et al*, Appl. Phys. Lett. **70**, 1747(1997).
- [2.45] D. M. Feldmann and D. C. Larbalestier, Appl. Phys. Lett. **83**, 3951(2005).
- [2.46] J. A. Smith, M. J. Cima, and N. Sonnenberg, IEEE Trans. Appl. Supercond. **9**, 1531(1999).
- [2.47] A. I. Larkin and Yu. Ovchinnikov, J. Low Temp. Phys. **21**, 409(1979).

[2.48] R. Feenstra *et al.*, Presented in DOE Peer Review 2003.

CHAPTER 3

[3.1] X. Wang and J. Z. Wu, Physica C **432**, 287(2005).

[3.2] C. P. Bean, Rev. Mod. Phys. **36**, 31 (1964).

[3.3] This scaling behavior is observed at 77 K and SF by measuring samples from a same batch with these two techniques.

[3.4] M. Varela, Z. Sefrioui, and D. Arias *et a.*, Phys. Rev. Lett. **83**, 3936(1999).

[3.5] W. J. Lin, P. D. Hatton, F. Baudenbacher and J. Santiso, Appl. Phys. Lett. **72**, 2966(1998).

[3.6] U. Welp, W. K. Kwok, G. W. Crabtree, K. G. Vandervoort, and J. Z. Liu, Phys. Rev. Lett. **62**, 1908(1989).

[3.7] M. Tinkham, Phys. Rev. Lett. **61**, 1658(1988).

[3.8] C. J. Can der Beek and M. Konczykowski, Phys, Rev. B **66**, 024523(2002).

[3.9] A. O. Ijaduola, J. R. Thompson, R. Feenstra, D. K. Christen, A. A. Gapud and X. Song, Phys. Rev. B **73**, 134502(2006).

[3.10] E. Sheriff, R. Prozorov, Y. Yeshurun, and A. Shaulov, J. Appl. Phys. **82**, 4417(1997).

[3.11] Qiang Li, M. Suenaga, Z. Ye, S. R. Foltyn, and H. Wang, Appl. Phys. Lett. **84**, 3528(2004).

[3.12] C. Cai, B. Holzapfel, J. Hänisch and L. Schultz, Phys, Rev. B **70**, 064504(2004).

[3.13] A. Gurevich, Supercond. Sci. Technol. **20** (2007) S1–S8.

[3.14] K. Verbist, A. Kule and A. Vassiliev, Physica C **269**, 131(1996).

[3.15] T. I. Selinder, U. Helmersson, Z. Han, J. E. Sundgren, H. Sjöström, and L. R.

Wallenberg, Physica C **202**, 69(1992).

[3.16] A. Catana, R. F. Broom, J. G. Bednorz, J. Mannhart, and D. G. Schlom, Appl. Phys. Lett. **60**, 1016 (1992).

[3.17] Chang Jun Liu and Claire Schlenker, Phys, Rev. B **48**, 13911(1993).

[3.18] A. Gurevich, 2004 presented at the Annual DOE Peer Review, July 28, Washington DC.

CHAPTER 4

[4.1] Ivar Giaever, Phys. Rev. Lett. **15**, 825(1965).

[4.2] J. Pearl, Appl. Phys. Lett. **16**, 50(1966).

[4.3] J. R. Clem, Phys, Rev. B. **12**, 1742(1975).

[4.4] K. A. Delin and A. W .Kleinsasser, Supercond. Sci. Technol. **9**, 227(1996).

[4.5] S. Berger, K. Bouzehouane, D. Crete and J. –P. Contour, Eur .Phys. J. AP **6**, 111(1999).

[4.6] S. R. Foltyn, H. Wang, L. Civale et al, Appl. Phys. Lett. **87**, 162505(2005).

CHAPTER 5

[5.1] Judy Z. Wu, R. L. S. Emergo, Xiang Wang *et al.*, Appl. Phys. Lett. **93**, 062506(2008)

[5.2] R. L. S. Emergo, J. Z. Wu, T. J. Haugan and P. N. Barnes, Preprint.

[5.3] G. W. Xu and J. Z. Wu, Preprint.

[5.4] B. W. Kang, A. Goyal, D. R. Lee, J. E. Mathis, E. D. Specht, P. M. Martin, D. M. Kroeger, M. Paranthaman, and S. Sathiyamurthy, J. Mater. Res. **17**, 1750 (2002).

[5.5] S. R. Foltyn, L. Civale, J. L. Macmanus-Driscoll, Q. X. Jia, B. Maiorov, H. Wang and M. Maley, Nature Mater. **6**, 631 (2007).

- [5.6] C. J. Van der Beek, M. Konczykowski, A. Abaloshev ,I. Abalosheva, P. Gierlowski, S. J. Lewandowski, M. V. Indenbom, and S. Barbanera, Phys. Rev. B **66**, 024523(2002).
- [5.7] X. Wang and J. Z. Wu, Phys. Rev. B **76**, 184508 (2007).
- [5.8] A. O. Ijaduola, J. R. Thompson, R. Feenstra, D. K. Christen, A. A. Gapud and X. Song, Phys. Rev. B **73**, 134502(2006).
- [5.9] T. L. Hylton and M. R. Beasley, Phys. Rev. B **41**, 11669 (1990).
- [5.10] M. Tinkham, “*Introduction to Superconductivity*”, 2nd edition, (McGraw-Hill, New York, 1996).

CHAPTER 6

- [6.1] S. Kang, A. Goyal and J. Li *et al*, Science **311**, 1911(2006).
- [6.2] T. J. Haugan, P. N. Barnes, T. A. Campbell *et al*, IEEE Trans. Appl. Supercond. **17**, 3724(2007).
- [6.3] J. Gutiérrez, A. Llordés, J. Gázquez *et al*, Nature Materials **6**, 367(2007).
- [6.4] A. Goyal, D. K. Christen and M. Paranthaman, Presented in DOE Peer Review 2006.
- [6.5] C. V. Varanasi, J. Burke, and L. Brunke *et al*, J. Appl. Phys. **102**, 063909(2007).
- [6.6] C. V. Varanasi, P. N. Barnes and J. Burke, Supercond. Sci. Technol. **20**, 1071(2007).
- [6.7] R. L. Emergo, J. F. Baca and J. Z. Wu, Preprint.
- [6.8] X. Wang and J. Z. Wu, Physica C **432**, 287-292(2005).

PUBLICATIONS

1. Judy Z. Wu, R.L.S. Emergo, Xiang Wang, G. W. Xu, T. J. Haugan and P. N. Barnes, “*Strong nanopore pinning enhances J_c in $YBa_2Cu_3O_{7-x}$ films*”, Applied Physics Letters **93**, 062506(2008)
2. Hua Zhao, Xiang Wang and Judy Z. Wu, “*Effect of Magnetic Pinning on Microwave Nonlinearity in High Temperature Superconductor Thin Film Band-Pass Filters*”, Superconductor Science and Technology **21**, 085012(2008)
3. Xiang Wang and Judy Z. Wu, “*Eliminating J_c thickness dependence in $YBa_2Cu_3O_{7-x}$ films using nanotube insertion*”, Physical Review B **77**, 144525(2008) (selected for the Virtual Journal of Applications of Superconductivity)
4. Xiang Wang and Judy Z. Wu, “Effect of temperature and magnetic field on the thickness dependence of the critical current density of $YBa_2Cu_3O_{7-x}$ films”, Physical Review B **76**, 184508(2007) (selected for the Virtual Journal of Applications of Superconductivity)
5. Jonathan R. Dizon, Xiang Wang, Roberto S. Aga, Jr., and Judy Z. Wu, “Combining near-field scanning microwave microscopy with transport measurement for imaging current-obstructing defects in HTS films”, IEEE Transactions on Applied Superconductivity, Vol. 17, No.2, 3219(2007)
6. Xiang Wang and Judy Z. Wu, “Effect of interlayer magnetic coupling on the $YBa_2Cu_3O_7$ /insulator/ $YBa_2Cu_3O_7$ trilayers”, Applied Physics Letters **88**, 062513(2006) (selected for the Virtual Journal of Applications of Superconductivity)

7. Xiang Wang and Judy Z. Wu, “Tailoring defect microstructure for better magnetic flux pinning in YBa₂Cu₃O_{7-δ} films using quench annealing”, *Physica C* 432, 287-292(2005)
8. Roberto S. Aga, Jr., Xiang Wang, Jonathan Dizon, Jesse Noffsinger, and Judy Z. Wu, “Application of near-field scanning microwave microprobe to electrical current density mapping”, *Applied Physics Letters* 86, 234101(2005) (selected for the *Virtual Journal of Applications of Superconductivity*).
9. Judy Z. Wu, Xiang Wang, R.L.S. Emergo and A. Dibos, “Aligned Nanotube as strong magnetic flux pins in superconducting YBa₂Cu₃O_{7-δ} films”, in preparation.
10. Xiang Wang, Javier F. Baca and Judy Z. Wu, “The effect of strong linear defects on J_c–thickness dependence”, in preparation.